Revealing Hidden Oxygen Variability in the North Pacific: A Two-Decade Analysis Using GOBAI-O_2

Miho Ishizu[1, 2], Tomomichi Ogata[3]

[1]*Center for Climate Physics, Institute for Basic Science, Busan 46241, Republic of Korea*

[2]*Pusan National University, Tonghapgigyegwan Bldg 2 Busandaehak-ro, 63 beon-gil, Geumjeong-gu, Busan 46241, Republic of Korea*

[3]*Japan Agency for Marine-Earth Science and Technology, Environmental Variability Prediction and Application Research Group, Yokohama Institute for Earth Sciences, 3173-25 Showa-machi, Kanagawa-ku, Yokohama 236-0001, Japan*

To whom correspondence may be addressed. Email: mishizu@pusan.ac.kr

Abstract

Oceanic dissolved oxygen concentrations are thought to be declining under ongoing global warming, yet their variability remains less well understood than that of physical parameters such as temperature and salinity, primarily due to the limited spatial and temporal coverage of oxygen observation. Here, we examine linear trends in potential temperature, salinity, and dissolved oxygen in the North Pacific over the past two decades (2004–2023), using the GOBAI-O_2 dataset. We compare the diagnosed oxygen trends with those of physical parameters to reveal the spatial structure of recent changes. The oxygen trends inferred from GOBAI-O_2 are broadly consistent with trends observed along ship-based hydrographic repeat lines. While basin-scale deoxygenation is evident, we also identify localized oxygen increases on specific density surfaces. By relating these patterns to the surrounding physical

environment, we find that the spatial heterogeneity in oxygen trends is consistent with known oceanographic processes, including the southward retreat of the oxygen minimum layer and the northward migration of a front separating the subtropical and subarctic gyres. These results underscore the value of GOBAI-O_2 data in linking physical variability to previously unrecognized biological and biogeochemical patterns in the ocean.

Plain Language Summary

1. We investigated how potential temperature, salinity, and dissolved oxygen have changed in the North Pacific over the past 20 years using GOBAI-O_2 dataset, and we examined the physical processes responsible for these trends.
2. The trends identified in this study are broadly consistent with findings from previous research, and improved spatial coverage of GOBAI-O_2 allowed us to reveal connections between regional patterns that we previously only partially understood.
3. Overall, dissolved oxygen decreased across much of the North Pacific. However, some regions showed increasing oxygen levels, indicating that the changes were not uniform. These non-uniform patterns reflect known physical ocean processes. For example, higher oxygen levels in the northern North Pacific are consistent with a northward shift of the front separating the subtropical and subarctic gyres. In the equatorial Pacific, the reduced westward extent of the oxygen minimum layer corresponds to a weakening and poleward shift of the North Equatorial Countercurrent (NECC) on interdecadal timescales.
4. These findings provide new evidence that links large-scale physical ocean changes to previously unclear changes in biological and biogeochemical observations.

Keywords: dissolved oxygen, 20-year linear trends, Bio-Argo float data, global warming

1. Introduction

Over recent decades, the global ocean has experienced a decline in its dissolved oxygen inventory, a trend projected to continue through the 21st century [Keeling et al., 2010; Breitburg et al., 2018; Stramma and Schmidtko, 2021; Limburg et al., 2020; Ito et al., 2017, 2024; Kolodziejczyk et al., 2024]. This deoxygenation is driven in part by reduced ocean oxygen solubility under rising sea-surface temperatures, which promotes oxygen outgassing. In addition, enhanced stratification and a slowdown of ocean circulation under global warming can reduce interior ventilation and oxygen supply [Keeling et al., 2010, Bopp et al. 2013; Ito et al. 2017]. Ocean oxygen loss can negatively affect aerobic marine organisms [Pörtner and Farrell, 2008; Sampaio et al., 2021], alter biogeochemical cycles, and potentially induce climate-relevant feedback [Berman-Frank et al., 2008]. Historical deoxygenation has been inferred from globally distributed observations [Helm et al., 2011; Schmidtko et al., 2017; Ito et al., 2017; Takatani et al., 2012; Sasano et al., 2015; Lauvset et al., 2022b], and Earth system models have been used to simulate both historical and future changes in ocean oxygen [Bopp et al., 2013; Kwiatkowski et al., 2020; Li et al. 2020].

Observed oxygen trends have traditionally been assessed using the discrete measurements of dissolved oxygen concentration (O_2), typically obtained by Winker titration [Winkler, 1988]. These measurements are also used to calibrate electrode- and more recently, optode-based oxygen sensors mounted on conductivity-temperature-depth (CTD) profilers [Helm et al. 2011; Schmidtko et al., 2017; Lauvset et al., 2022b]. Although programs such as WOCE, CLIVAR, and GO-SHIP have collected high-quality oxygen measurements globally, repeat occupation intervals are commonly on the order of a decade, limiting the ability to robustly quantify annual to seasonal variability. Higher-

frequency ship-based observations exist in a few regions [Takatani et al. 2012; Sasano et al., 2015], but their spatial coverage is limited. Consequently, despite attempts to characterize basin-scale pattern [Ito et al. 2017; Stramma et al. 2020; Kolodziejczyk et al. 2024], observational constraints have hampered a spatially and temporally comprehensive understanding of dissolved oxygen variability and trends.

Oxygen sensors were first deployed on Argo profiling floats in the mid-2000s. Since then, approximately 1,800 oxygen-equipped floats have been deployed worldwide, substantially advancing the observational basis for assessing oxygen variability and trends [Sharp et al., 2023]. The expansion toward a global biogeochemical (BGC) Argo network has improved sampling in regions that were previously sparsely observed [Claustre et al., 2020]. In parallel, major progress has been made in calibration, adjustments, and quality control of oxygen measurements, including pre-deployment drift corrections [D'Asaro and McNeil, 2013; Johnson et al., 2015; Bittig and Körtzinger, 2015; Bushinsky et al., 2016; Drucker and Riser, 2016; Nicholson and Feen, 2017], climatology-based calibrations [Takeshita et al., 2013], in-air oxygen measurement calibrations [Körtzinger et al., 2005; Bittig and Körtzinger, 2015; Johnson et al., 2015; Bushinsky et al., 2016], post-deployment drift corrections [Johnson et al., 2017; Bittig et al., 2018a, b], and the standardized delayed-mode quality control procedures [Maurer et al., 2021]. Together, these developments have reduced uncertainty and improved the consistency of optode-based [O_2] measurements from Argo floats.

To date, oxygen observations from Argo floats have been used primarily in regional process studies, including air-sea oxygen exchange [Wolf et al., 2018], upper-ocean primary production [Alkire et al., 2012; Estapa et al., 2019], biological pump efficiency [Johnson and Bif, 2021], and the dynamics of the oxygen minimum zone [Udaya Bhaskar et al., 2021]. Recently, Sharp et al. [2023] produced a

four-dimensional gridded [O_2] product, GOBAI-O_2 (Gridded Ocean Biogeochemistry from Artificial Intelligence (AI) – Oxygen). GOBAI-O_2 is constructed using machine-learning methods trained on oxygen observations and designed to reconstruct spatial patterns, seasonal cycles, and decadal variability, particularly in regions where observational data gaps coincide with high background O_2 variability.

In the North Pacific, several studies have documented heterogeneous oxygen trends. Using an objectively mapped monthly climatology of O_2 based on the World Ocean Database 2013 (WOD13) [Boyer et al. 2013], Ito et al. [2017] reported multidecadal variability and trends in dissolved O_2 in the surface-layer oxygen from 1958 to 2013. Sasano et al. [2015], using the high-frequency shipboard sections along the 137°E and 165°E lines from 1987 to 2011, reported oxygen declines in the northern subtropical to subtropical-subarctic transition zones of -0.45 ± 0.16 μmol/kg/yr at 25.3 σ_θ and -0.45 ± 0.14 μmol/kg/yr at 26.8 σ_θ, respectively. They also identified a significant oxygen increase in the tropical Oxygen Minimum Layer (OML) of +0.36 ± 0.004 μmol/kg/yr, highlighting pronounced spatial heterogeneity. At broader scales, Stramma et al. [2020] analyzed historical bottle data and reported links between oxygen variability and climate modes such as the Pacific Decadal Oscillation (PDO) and the North Pacific Gyre Oscillation (NPGO), although sparse sampling makes it difficult to robustly connect regional trends to physical mechanisms. Collectively, previous studies indicate that oxygen changes in the North Pacific can be strong, spatially non-uniform, and potentially driven by both circulation/ventilation changes and biologically mediated oxygen consumption [Sasano et al. 2015; 2018; Ito et al. 2017; 2024; Stramma et al., 2020; Kolodzijejczyk et al. 2024].

Because observational opportunities to quantify trends in dissolved oxygen–together with concomitant changes in temperature and salinity–remain limited, gridded products such as GOBAI-O_2 are becoming increasingly valuable for basin-scale analyses. In this study, we use GOBAI-O_2 to quantify

linear trends in potential temperature, salinity, and dissolved oxygen in the North Pacific over 2004–2023 and examine how their trends are connected in both depth and density space. We further discuss the extent to which the diagnosed oxygen trends can be interpreted in terms of physical drivers, including surface warming, stratification changes, and circulation variability in the North Pacific.

2. Data and Methods

2.1 GOBAI-O_2 dataset

We use GOBAI-O_2, a four-dimensional, monthly gridded product of dissolved oxygen (O_2) in the ocean interior, generated using machine learning (ML) algorithms trained on both Argo float oxygen measurements and ship-based discrete observations [Sharp et al., 2023]. GOBAI-O_2 is mapped onto the temperature- salinity fields provided by the global Argo array [Roemmich and Gilson, 2009]. The underlying oxygen training database combines ship-based measurements from GLODAPv2.2022 and Argo float data distributed through the Argo Global Data Assembly Centers, after quality control [Sharp et al., 2023] (https://doi.org/10.25921/z72m-yz67).

The ML models predict O_2 using predictors that include absolute salinity, conservative temperature, potential density anomaly, hydrostatic pressure, bottom depth, and additional spatiotemporal covariates representing geographic, seasonal, and interannual variability. Biological processes are not explicitly parameterized in the ML framework; however spatiotemporal covariates can implicitly capture biological influences to some extent [Giglio et al., 2018].

GOBAI-O_2 is produced using two ML approaches: feed-forward networks (FNNs) and random forest regression (RFRs, [Breiman, 2001]). The final O_2 estimate at each grid point is taken as the mean of the FNN and RFR predictions. The dataset spans 2004–2023 at monthly resolution on a 1° × 1°

147 latitude –longitude grid, covering 86% of the global ocean area. The product is provided on 58 vertical
148 levels from the surface to ~2,000 m. Sharp et al. [2023] reported 0.79 ± 0.04% per decade decrease
149 in the oxygen inventory of the upper 2000 m over 2004–2022. Full details of their data sources,
150 processing, algorithm training, evaluation, and uncertainty estimation are given in Sharp et al. [2023].

151

152 **2.2 Uncertainty estimates**

153 GOBAI-O_2 provides an uncertainty estimate for each gridded O_2 value, constructed by combining
154 independent uncertainty components in quadrature [Sharp et al., 2023]:

155 $$u([O_2])_{tot.} = \sqrt{u([O_2])^2{}_{meas.} + u([O_2])^2{}_{grid.} + u([O_2])^2{}_{alg.}} \quad (1),$$

156 where $u([O_2])^2{}_{meas.}$ represents measurement uncertainty of the underlying observations,
157 $u([O_2])^2{}_{grid.}$) is the gridding uncertainty associated with representing a four-dimensional
158 spatiotemporal volume by a single value, and $u([O_2])^2{}_{alg.}$ is the algorithmic uncertainty arising from
159 the ML estimation. We use $u([O_2])_{tot.}$ to characterize uncertainty in O_2 and to propagate uncertainty
160 into our oxygen trend estimates (Figs. 1–4). In most figures, we incorporate the mean uncertainty when
161 estimating linear O_2 trends.

162

163 **2.3 Vertical grid and interpolation for isopycnal analysis**

164 GOBAI-O_2 is provided on a 1° × 1° horizontal grid with 58 depth levels: 2.5, 10, 30, 40, 50, 60, 70,
165 80, 90, 100, 110, 120, 130, 140, 150, 160, 170, 182.5, 200, 220, 240, 260, 280, 300, 320, 340, 360,
166 380, 400, 420, 440, 462.5, 500, 550, 600, 650, 700, 750, 800, 850, 900, 950, 1000, 1050, 1100, 1150,
167 1200, 1250, 1300, 1350, 1412.5, 1500, 1600, 1700, 1800, 1900 and 1975 m. The enhanced near-surface
168 vertical resolution is important for resolving strong gradients in temperature, salinity, density, and
169 oxygen within the mixed layer [Kara et al., 2000].

For analysis performed in density space, we interpolate the original depth-level data to 1-m vertical grid using cubic spline interpolation and then evaluate linear trends on a 1° × 1° × 1 m grid. This approach enables computation of trends as a function of latitude (1° bins) and potential density anomaly ($0.1\sigma_\theta$ bins) (Figs. 4–7). To evaluate sensitivity to interpolation choices, we repeated the analysis using linear, shape-preserving cubic (PCHIP) interpolation and using coarser vertical grids (2m and 5m). The resulting trend patterns show no material differences among interpolation methods (Figs. S1 (a, b) and S2 (a, b)). The 5-m grid cannot resolve densities lighter than $24.0\sigma_\theta$ at some latitudes; however, the main features are preserved across all tested resolutions.

2.4 OFES model output

In Section 3.3.2, we additionally use output from the eddy-resolving OGCM for the Earth Simulator (OFES) [Masumoto et al., 2004; 2010; Sasaki et al., 2008] to examine the physical context of the diagnosed variability. OFES is based on the MOM3 [Pacanowski and Griffies, 2000] and uses a quasi-global domain spanning 75° S– 75°N with 0.1° x 0.1° horizontal resolution and 54 vertical levels. The model was initialized from rest using the World Ocean Atlas 1998 (WOA98) [Boyer and Levitus, 1997], and spun up for 50 years using climatological forcing derived from NCEP-NCAR reanalysis [Kalnay et al., 1996]. After spin-up, a hindcast experiment was conducted from 1950 to 2024 using daily NCEP-NCAR forcing. Here we analyze OFES output over1950–2023.

3. Results

3.1 Horizontal distributions of linear trends

Figure 1 illustrates the horizontal and vertical distributions of linear trends in potential temperature, salinity, and dissolved oxygen (O_2), over 2004–2023. Positive trends in potential temperature are

primarily confined to the surface layer above 200 m depth (Fig. 1a–c), with larger magnitudes at higher latitudes. In contrast, negative trends emerge below the surface in the eastern tropical area (180°–120°W, 5°–15°N) (Fig. 1b), extending westward and deepening with increasing depth (Fig. 1d–f). Below ~400 m, the spatial distributions of positive and negative temperature trends differ between the subarctic and subtropical gyres.

Salinity trends exhibit generally negative values throughout the surface layer (Fig. 1h–i), consistent with freshening. Localized positive salinity trends are detected in the Kuroshio–Oyashio transition area and the northwest Pacific (140°–180°E, 20°–50°N), as well as in the tropical region (120°–170°E, 0°–10°N). Additional positive trends appear along the eastern boundary off California (130°–199°W, 20°–40°N). Below 200 m depth, salinity trends are weaker and broadly mirror the temperature ones (Fig. 1j–k). Notably, negative salinity trends are evident around the Alaska gyre (170°–130°W, 40°–55°N) (Fig. 1j–l), a pattern that differs from the corresponding temperature trends.

Negative trends in dissolved O_2 are widespread across the North Pacific and extend throughout much of the water column (Fig. 1o–u). Large negative trends are concentrated at higher latitudes near the surface, with their locations shifting systematically with depth. Particularly strong O_2 declines are observed along the northeastern boundary (140°–130°W, 40°–50°N) and within the southern subtropical region (10°–25°N) on density surfaces between 25.2 and 26.8σ_θ, corresponding to depths of approximately 200–600 m (Fig. 1q–s). In contrast, weak positive O_2 trends are detected below 200 m depth in the Kuroshio–Oyashio transition zone (130°–150°E, 30°–40°N), extending into deeper layers and spreading northeastward across the basin (Fig. 1r–u).

Positive O_2 trends are restricted to specific regions and depths: the tropical region at ~100 m depth

(Fig. 1p); the Alaska Gyre at 200–400 m depth (Fig. 1q–r); the western tropical region at 400–600 m depth (Fig. 1r–s); and the Kuroshio–Oyashio transition region at similar depths (Fig. 1r–s). When examined as a function of latitude, the magnitudes of negative O_2 trends do not depend monotonically on latitude alone. While surface-layer declines are strongest at high latitudes, the largest negative trends at intermediate depths (400–600m) occur in the mid-latitude band (30°–40°N). This depth-dependent latitudinal structure implies the importance of remote transports and the circulation-driven redistribution of oxygen, rather than purely local surface forcing. The underlying mechanisms are discussed further in Section 3.3.

The total uncertainty in dissolved O_2, $u([O_2])_{tot.}$, exhibits pronounced regional structure (Fig. 1v–bb). Uncertainty is largest in the North Pacific north of 50°N and decreases toward lower latitudes. Relatively high uncertainty values are also evident in the surface layer, and within regions of strong density gradients in the eastern tropical Pacific [150°–120°W, 10°–30°N] at depths of 100–200 m (Fig. 1w–x). In general, uncertainty peaks near 100 m depth and decreases with increasing depth (Fig. 2 and Figure A14 in Sharp et al. [2023]). As shown by Sharp et al. [2023], regionally variations in uncertainty are dominated by algorithmic uncertainty rather than measurement or gridding components (Eq. 1). Elevated algorithmic uncertainty in the northern Pacific above 50°N and along the western and eastern tropical margins below 20°N reflects sparse observational coverage in these regions (Figure 1 in Sharp et al. 2023).

Compared with the historical horizontal distributions of dissolved O_2 reported by Ito et al. [2017] (Figure 3 in Ito et al. 2017), our analysis reveals a broader spatial extent of negative trends across the North Pacific. Whereas data gaps increase with depth in Ito et al. (2017), the GOBAI-O_2 product provides more spatially continuous coverage, yielding distributions that remain consistent with

242 surrounding regions. In addition, positive O_2 trend detected here in the Kuroshio-Oyashio transition
243 zone and the northeastern North Pacific on density surfaces of 26.8–27.0σ_θ (Fig. 1r) were not clearly
244 evident in the earlier climatology-based analysis. Similarly, the positive trends identified in the western
245 tropical Pacific below 400 m depth (Fig. 1r–t) are stronger and more spatially coherent than those
246 reported previously.

247

248 The positive O_2 trends coincide with regions of relatively low uncertainty values (Fig. 1p–s and 1w–
249 y), suggesting that they are robust features supported by the high observation density of Argo profiling
250 floats. Other regions exhibiting positive signals—the northeastern North Pacific with a density range
251 of 26.8–27.0σ_θ (170°E–150°W, 45–55°N, Fig. 1r) and the tropical western Pacific (130°–170°E, 0°–
252 10°N, Fig. 1r–t)—also correspond to areas of low uncertainty (Fig. 1y-aa). Consequently, these
253 signals likely represent genuine regional reoxygenation superimposed on the basin-scale
254 deoxygenation trend.

255

256 Some localized expansions of the trends, particularly in the tropical eastern Pacific (e.g. 170°–130°W,
257 0°–20°N) may partly reflect regions of elevated uncertainty, occasionally exceeding 15 μmol/kg (Fig.
258 1q–s; Fig. 4i). Such large uncertainties arise from sparse observations and high background variability
259 [Sharp et al. 2023]. Additional bias may stem from sensor calibration limitations in Argo oxygen
260 measurements, especially in oxycline regions where finite optode response times can introduce
261 systematic errors [Bittig et al., 2014; 2018a,b]. Despite these caveats, the spatial patterns of the
262 diagnosed O_2 trends are generally smooth and coherent across the basin. Based on statistical
263 significance testing, most trends are significant throughout the water column (Fig. 1o–u), allowing
264 them to be interpreted in the context of established physical processes in the North Pacific. Overall,

the GOBAI-O_2 dataset provides an improved framework for diagnosing basin-scale oxygen variability and its physical drivers.

3.2 Vertical sections and isopyncal density analysis of liner trends in 137°E and 165°E lines

To facilitate direct comparison with historical ship-based observations, we examine vertical sections and isopycnal distributions of linear trends in potential temperature, salinity, and dissolved O_2 along the 137°E and 165°E meridional sections (Fig. 3). Ogata and Nonaka [2020] analyzed salinity data from 20 years of shipboard observations along the 137°E line between 1997 and 2016, while Sasano et al. [2015] analyzed temperature, salinity, and dissolved O_2 data from 25 years of cruises along the 165°E line between 1987 and 2011.

Along both sections, large negative trends in potential temperature and salinity are concentrated along the 25.0–26.0σ_θ isopycnal surfaces, corresponding to potential temperatures of approximately 10–12°C and salinities of 34.4–34.5 (Fig. 3a, b, e, f). In contrast, the strongest negative trends in dissolved O_2 occur primarily along denser isopycnals between 26.0 and 27.0σ_θ (Fig. 3c, g). This vertical separation indicates that the regions of pronounced oxygen decline are not co-located with those of temperature and salinity trends, implying distinct controlling mechanisms.

In addition to widespread oxygen declines, pronounced positive O_2 trends are detected south of ~15°N below 200 m depth along the 137°E line (Fig. 3c). These positive trends are located near the upper boundary of the oxygen minimum layer (OML). Comparison with the corresponding uncertainty distributions (Fig. 3d, h) shows that regions exhibiting positive or negative oxygen trends generally do not coincide with areas of elevated uncertainty, indicating that these signals are robust with the

GOBAI-O_2 framework.

The distributions of linear trends on isopycnal surfaces further highlight differences among temperatures, salinity, and dissolved O_2 (Fig. 4). Trends in temperature and salinity are closely aligned, with warming accompanied by salinification and cooling accompanied by freshening (Fig. 4a–b, d–e). In the tropical region (5°S–5°N), distinct positive trends in both variables are evident over the density range of 22.0–26.0σ_θ. In contrast, little systematic trend is detected in the salinity minimum region (S = 34–34.1) within the density range of 26.5–27.0σ_θ. At higher latitudes (40°–50°N), strong positive trends in both temperature and salinity are observed along the 26.0–27.0σ_θ surfaces (Fig. 4e).

Dissolved oxygen trends exhibit a markedly different structure. Although negative O_2 trends dominate overall, weak but coherent positive trends appear across the density range 23.0–26.0σ_θ in low-latitude regions (5°S–5°N). More pronounced positive O_2 trends are detected in the deeper density range of 26.0–27.0σ_θ between 5° and 10°N. Additional weak positive trends are observed between 10° and 20°N within the density range of 23.0–25.0σ_θ along both the 137°E and 165°E sections.

Compared with previous studies, the GOBAI-O_2-based trends reveal both similarities and notable differences. The general characteristics of temperature and salinity trends are broadly consistent with those reported by Sasano et al. [2015], although the present results are spatially smoother, particularly for dissolved oxygen. This smoothness likely reflects the gridded nature of the dataset and the spatial regularization inherent in the machine-learning reconstruction. Along the 137°E section, the GOBAI-O_2 temperature and salinity fields exhibit a wider area of negative salinity trends within the density range 22.0–24.0 σ_θ than those reported by Ogata and Nonaka [2020] using OFES output.

Ship-based observations by Sasano et al. [2015] identified patchy positive trends in oxygen within the density range 24.5–27.5σ_θ in the regions (5°–15°N and 6°S–1°N), as well as localized positive trends at greater depths. In contrast, the GOBAI-O_2 data reveal a broader, smoother, and more spatially coherent pattern of positive O_2 trend spanning -6°S to 5°N. At the same time, the present analysis more clearly delineates the core regions of negative oxygen trends between 5° and 15°N along the lower isopycnals (Fig. 3c and f), which are characteristic of the subtropical gyre. These differences underscore the complementary nature of ship-based observations and gridded reconstructions and highlight the advantage of GOBAI-O_2 for resolving basin-scale and isopycnal-scale oxygen variability.

3.3 Horizontal distribution of linear trends along isopycnal surfaces

3.3.1 Potential temperature and salinity

The horizontal distributions of linear trends in potential temperature, salinity, and dissolved oxygen on specific isopycnal surfaces at 25.0, 26.0, and 26.8σ_θ (Fig. 5) are illustrated to examine how these trends occur and how they are connected. These density surfaces correspond to the shallower density range of Subtropical Mode Water (STMW), the shallower densities of Central Mode Water (CMW) [Suga et al., 1997; 2004], and the representative density of North Pacific Intermediate Water (NPIW) [Nakamura et al., 2000a, b; Nakamura and Awaji, 2003; Yasuda, 2004], respectively. STMW is formed south of the Kuroshio Extension between 30–35°N and 130–170°E, and reaches depths of approximately 400 m in late winter. It then spreads toward the subtropical front through advection across the Kuroshio recirculation area. CMW is formed in the transition area of the central North Pacific and spreads eastward along the North Pacific Current before turning southward and westward in the subtropical gyre [Suga et al., 1997; 2004]. In contrast, NPIW does not outcrop during its formation process. Its origin lies in Okhotsk Sea Mode Water, which forms through overturning driven by diapycnal upwelling and tidal mixing around the Kuril Islands [Nakamura et al., 2000a, b;

336 Nakamura and Awaji, 2003; You, 2003; Yasuda, 2004] as well as double diffusions in the North Pacific
337 [You, 2003].
338
339 The linear trends on the 25.0, 26.0, and 26.8σ_θ surfaces show that positive and negative tendencies
340 appear in characteristic locations and are generally aligned with the geostrophic streamlines (Fig. 5a–
341 b, d–e, g–h). Although exceptions exist, such as weak positive trends (150–175°E, 20–30°N) (Fig.
342 5a–b), negative trends in potential temperature and salinity dominate in the western and central North
343 Pacific on the 25.0 and 26.0$\sigma_\theta$surfaces (Fig. 5a–b, d–e). Conversely, positive trends in temperature
344 and salinity are most prevalent in the northeastern and/or eastern regions of the basin along the
345 geostrophic streamlines (Fig. 5a–b, d–e). These patterns suggest that waters subducted in the frontal
346 region with reduced temperature and salinity originate mainly from the northeastern North Pacific and
347 are advected southward along the subtropical circulation (Fig. 5a–b, d–e). Exceptions occur in parts
348 of the northeastern basin (170–130°W, 40–60°N), where warmer and more saline waters influence
349 the water masses sinking near the Alaska gyre and subsequently transported outside the subtropical
350 gyre and along the California coast.
351
352 At 26.8σ_θ (Fig. 5g–h), large positive trends in temperature and salinity are found along the Kuril
353 Islands, with moderate positive trends appearing on the eastern side of the basin, respectively. Waters
354 at this density range (26.8σ_θ) are not directly ventilated but are formed through diapycnal mixing
355 processes [Nakamura et al., 2000a, b; Nakamura and Awaji, 2003; You, 2003; Yasuda, 2004] and
356 through double diffusion such as salt finger [You, 2003]. Thus, the observed positive temperature and
357 salinity trends at 26.8σ_θ likely reflect influences from changes occurring in the overlying layers (Fig.
358 5d–e and g–h).
359

A meridional northward shift of the outcrop line in the North Pacific associated with recent climate change has been identified in OFES analyses [Ogata and Nonaka, 2020]. Similar northward shifts of 25.0 and 26.0σ_θ outcrop lines appear in the present dataset (Fig. 6). These northward displacements can be attributed to surface warming and increased stratification under global climate change and provide an explanation for negative temperature and salinity trends observed in the subtropical gyre, where less saline subarctic-origin waters are subducted and advected southward. The positive temperature and salinity trends occurring in the Alaska region [160°–130°W, 30°–60°N] (Fig. 5a–b and d–e) are also consistent with the direct warming effect. The 26.0σ_θ front exhibits primarily longitudinal, rather than meridional, shifts between 2004 and 2023 (Fig. 6), suggesting that the corresponding temperature and salinity changes arise directly from surface warming and freshening, rather than from density-compensated shifts in water-mass distribution.

3.3.2 Dissolved oxygen

The linear trends in dissolved oxygen on the isopycnal surfaces at 25.0, 26.0, and 26.8σ_θ exhibit predominantly negative values across the North Pacific (Fig. 5c, f, and i), although their spatial distributions are not uniform. Large negative trends are concentrated in the northeastern and eastern regions and gradually decrease toward the west (Fig. 5q, f, and i). Exceptions occur mainly in the tropics, where notable positive trends in the western tropical areas on the 26.0 and 26.8σ_θ surfaces.

The temporal changes in dissolved oxygen (O_2) were decomposed following the method of Sasano et al. [2015]. The processes underlying the oxygen tendency equations (Eqs. 2 and 3) are summarized below. We evaluated each contributing term and examined its relative importance for the dissolved O_2 trends. The total tendency of dissolved oxygen can be expressed as

$$\frac{\partial O_2}{\partial t} = \left(\frac{\partial O_2}{\partial z}\frac{\partial z}{\partial t}\right) + \left(\frac{\partial O_2^{sat}}{\partial t}\right)_{net} - \left(\frac{\partial (AOU)}{\partial t}\right)_{net}, \quad (2)$$

which can be rearranged as

$$\frac{\partial O_2}{\partial t} = \left(\frac{\partial O_2}{\partial z}\frac{\partial z}{\partial t}\right) + \left(\frac{\partial O_2^{sat}}{\partial t} - \frac{\partial O_2^{sat}}{\partial z}\frac{\partial z}{\partial t}\right) + \left(-\frac{\partial (AOU)}{\partial t} + \frac{\partial (AOU)}{\partial z}\frac{\partial z}{\partial t}\right). \quad (3)$$

(i) (ii) (iii) (iv) (v) (vi)

Here, $X = O_2$, O_2^{sat}, AOU (Apparent Oxygen Utilization). The term $\partial z/\partial t$ denotes the temporal change in the depth of the isopycnal surface (z), while $\partial X/\partial z$ represents the vertical gradient of the variable X at that surface, averaged over the past 20 years. The net tendency term ($\partial X/\partial t$)$_{net}$ represents the net changes associated with a variable X.

By applying Eq. (3), the rate of O_2 change (term i), which is the rate of reconstructed O_2 data estimated from the linear regression analysis, on each isopycnal surface can be decomposed into contributions from:

(term ii) vertical heave acting on the vertical O_2 gradient;

(term iii) solubility effects due to temperature and salinity changes;

(term iv) vertical heave acting on the solubility gradient;

(term v) AOU changes related to air-sea disequilibrium, biological activities, and lateral circulation

(term vi) vertical heave acting on AOU gradients.

The derivation of Eqs. (2) and (3) follows Sasano et al. [2015] and is described in Appendix. A schematic illustration of this decomposition is provided in Supplementary Figure S5.

Figure 7 shows the horizontal distributions of the magnitude of each term on 25.0σ_θ, 26.0σ_θ, and 26.8σ_θ surfaces. The results indicate that the prominent O_2 declines (Fig. 5c, f, i) arise from a combination of positive and negative contributions, with the dominant terms varying by latitude. In the high-latitude

region around the Alaska Gyre in higher latitudes (170°–130°W, 40°–60°N), the largest negative contributions are associated with the deepening of isopycnal surfaces (term ii) and the vertical heave acting on the AOU gradient (term vi) (Fig. 7f, j, k, o). Because the dissolved oxygen generally decreases with depth ($\partial O_2/\partial z < 0$), deepening of isopycnal surfaces ($\partial z/\partial t > 0$) (Fig. 8 b–c) produces a negative contribution through vertical heave. Similarly, because AOU typically increases with depth, isopycnal deepening leads to an apparent increase in AOU, contributing negatively to dissolved O_2 via term (vi). In contrast, solubility-related changes (term iii) and net AOU tendencies (term v) act in opposite directions during this period (Fig. 7g–h, l–m). Taken together, these results are consistent with the strong negative O_2 trends observed in the Bering Sea on the $26.0\sigma_\theta$ and $26.8\sigma_\theta$ surfaces (150°E–170°W, 50–60°N; Figs. 5f and i).

In the subtropical and mid-latitudes (10°–40°N), the O_2 decline is largely associated with AOU changes (term v) (Fig. 7d, i, and n). The relative weakening of the total O_2 decrease in the western North Pacific (Fig. 5c, f, i) coincides with positive contributions from vertical heave of isopycnal surfaces (term ii) (Fig. 7f and k). Additional positive trends arise from solubility-related effects (term iii) (Fig. 7b), and the vertical heave acting on the AOU gradient (term vi) (Fig. 7j and o and Fig. 8b–c).

In the mid-ocean between 170°E and 160°W, the positive O_2 tendencies transition to weakly negative values. In contrast, a pronounced band of positive trends zonally across the North Pacific Ocean between 30°N and 50°N, primarily associated with the combined effects of terms (iii) and (v) (Fig. 7l, h–i, and m–n). This pattern may be related to the northward meridional shift of the subtropical and subarctic frontal zone under recent global warming [Ogata and Nonaka, 2020]. Enhanced winter

convection in this region may introduce nutrients into the surface layer, potentially increasing biological activity and AOU. In the NPIW formation region near the Kuril Islands, negative contributions from term (iii) are observed (Fig. 7l), suggesting weaker vertical mixing during the observational period, likely influenced by enhanced surface-layer stratification. This interpretation is supported by the positive trends in temperature and salinity observed in the winter subducted areas [Suga et al., 1997; 2004; Yasuda, 2004] (Fig. 5d–e, g–h).

In the western tropical Pacific, pronounced increases in dissolved O_2 are observed within the density range of 26.8–27.2 σ_θ (Fig. 3c and g; Fig. 4c and g; Fig. 5c, f, and i), overlapping with the OML [Reid, 1997]. Similar features have been reported by Sasano et al. [2015] and Takatani et al. [2012]. Variability of the North Equatorial Counter Current (NECC) is likely relevant in this region. According to the study of Chen et al. [2016] based on the OFES outputs including a multidecadal variability (1960–2014), the NECC exhibits two distinct modes of variability: an interannual mode characterized by strengthening accompanied by southward migration, and an interdecadal mode marked by a gradual weakening, poleward migration, and broadening.

The validity of time-varying signals in the western tropical Pacific in the OFES data has been demonstrated by Chen et al. [2016]. We further examined the longer-term OFES data (1950–2023), as well, for poleward, eastward velocities, as well as potential temperature and salinity here (Fig. 9c, g). Positive temperature anomalies in 0°–5 °N occur above 250 m depth, while negative anomalies appear along the 26.0σ_θ surface between 5°–20°N, a similar pattern that is also evident in the GOBAI-O_2 data (Fig. 3a). A discrepancy is found in salinity trends: GOBAI-O_2 shows negative trends along

451 26.0σ_θ (Fig. 3b), whereas OFES exhibits positive trends (Fig. 9b, f), likely reflecting higher salinity
452 at 200–600 m depth in OFES between 0° and 7°N (Fig. 10b, d).

453

454 Anomalies in poleward and eastward velocities (Fig. 9a–b, e–f and Fig. 11a–b) indicate enhanced
455 poleward flow around 5°N above 200m depth and a poleward shift of the eastward velocity core. These
456 changes are consistent with the interdecadal mode of NECC variability described by Chen et al.
457 [2016]. The broadening of the NECC was less evident here, possibly because the present analysis
458 uses raw velocity fields rather than isolating the second EOF modes. The wind-stress curl over the
459 equatorial Pacific shows a persistent decrease and poleward expansion of negative values along the
460 0°–10°N from 1950 to 2023 (Fig. 12).

461

462 The westward penetration of the OML is slow and occurs between two eastward-extending tongues of
463 high O_2 water originating near the equator [Reid, 1997] (Fig. S6). The observed O_2 increase on the
464 26.8–27.2 σ_θ surfaces (Fig. 3c, g and Fig. 4c, g) is consistent with a weakening and north-poleward
465 shift of the interdecadal NECC mode. The subsurface O_2 increase, particularly below 400m depth (Fig.
466 1r–u), is therefore likely influenced by these circulation changes, potentially allowing higher-O_2 water
467 to extend westward (Fig. S6). In addition, shoaling of isopycnal surfaces near the equator indicates a
468 northward shift of the boundary between the tropical and subtropical gyres along 137°E line during
469 the observational period.

470

471 ## 4. Discussion and Conclusion

472 The variability of dissolved oxygen in the North Pacific reflects the combined influences of global

warming and climate variability. In this study, we used the four-dimensional GOBAI-O_2 dataset - constructed using machine -learning methods applied to historical temperature, salinity, and oxygen observations from BGC-Argo floats and ship-based measurements–to examine linear trends in potential temperature, salinity, and dissolved oxygen over the past two decades (2004–2023). The linear trends are broadly consistent with findings from previous studies [Takatani et al. 2012; Sasano et al. 2015; Ogata and Nonaka, 2020], and we clarified how these trends vary spatially (Figs. 3 and 4).

An important outcome of this study is that GOBAI-O_2, being globally gridded, allows spatially continuous and smooth representations of trends, both horizontally and vertically, across the North Pacific. This provides a more coherent picture than earlier datasets that relied solely on sparse ship-based observations. The horizontal trend patterns mapped on isopycnal surfaces (Fig. 5) show that dissolved oxygen exhibits a basin-scale decreasing trend. At the same time, several regions display locally increasing oxygen, including areas influenced by the meridional migration of subtropical and subpolar fronts (Fig. 4). The strong positive oxygen trends in the western equatorial region are consistent with a weakening of the second mode of the NECC variability. The decomposition analysis further illustrates how each physical component contributes to oxygen changes along isopycnal surfaces (Fig. 7).

Although many of the large-scale features identified here resemble those reported by Ito et al. [2017], our analysis reveals regional and isopycnal-scale structures that were previously unresolved. In particular, the positive oxygen trends in the Kuroshio–Oyashio Transition Zone, the northeastern North Pacific along the 26.8–27.0 σ_θ density surfaces, and the enhanced subsurface O_2 increase in the tropical western Pacific below 400 m were not clearly distinguished in earlier climatology-based studies. These

improvements arise because GOBAI-O_2 integrates high-frequency BGC-Argo oxygen observations with a spatially consistent mapping scheme, reducing observational gaps and sampling biases in dynamically active regions. This demonstrates that regional reoxygenation signals can coexist with large-scale deoxygenation, and highlights the importance of sustained BGC-Argo observations for detecting emerging changes in ocean biogeochemistry.

Recent work by Bushinsky et al. [2025] has reported the presence of a systematic negative bias (approximately -2.7 μmol kg^{-1}) in air-calibrated BGC-Argo oxygen measurements compared with ship-based reference profiles. This bias does not appear to be explicitly corrected in the GOBAI-O_2, and therefore may affect the magnitude of the estimated oxygen trends–potentially enhancing negative trends or suppressing positive ones in regions with dense float sampling. Such biases may also influence the apparent vertical structure of oxycline. In the North Pacific, regions with high float density–such as the Kuroshio–Oyashio transition zone, the North American coastal region, and the vicinity of Hawaii–may be particularly affected (see Fig. 1 of Sharp et al., 2023). While a constant offset would not directly alter linear trend estimates, any time–varying bias associated with sensor behavior or sampling depth could introduce spurious trends. A quantitative evaluation is not feasible at present due to the lack of temporally continuous ship-based reference data at the spatial scales. This limitation should therefore be kept in mind when interpreting the O_2 trends reported here.

It is also essential to recognize that GOBAI-O_2 is a machine learning reconstruction derived from available temperature, salinity, and oxygen measurements. While this approach significantly enhances special coverage, the results should be interpreted cautiously. Importantly, however, such methodological uncertainties are unlikely to alter the large-scale spatial coherence of the trend patterns identified in this study. Nevertheless, future work incorporating improved calibration of Argo oxygen sensors, expanded ship-based reference datasets, independent machine learning reconstructions [e.g.,

Ito et al., 2024], and comprehensive ocean reanalysis will be necessary to better constrain these uncertainties.

The monthly mean climatological GOBAI-O_2 data set should include the Pacific Decadal Oscillation (PDO; Stramma et al., 2020; Pozo Buil and Di Lorenzo, 2017) and the North Pacific Gyre Oscillation (NPGO; Stramma et al., 2020). This dataset, therefore, provides a valuable basis for examining how such climate variation influences dissolved oxygen through physical driving mechanisms. Investigating these relationships more explicitly will be an important direction for future research.

Data availability

GOBAI-O_2 data is available at https://www.ncei.noaa.gov/access/metadata/landing-page/bin/iso?id=gov.noaa.nodc:0259304. Temperature and salinity are from Roemmich and Gilson [2009] Argo climatology (https://sio-argo.ucsd.edu/RG_Climatology.html). The OFES and NCEP-NCAR data used in our study are obtained from APDRC, University of Hawaii (http://apdrc.soest.hawaii.edu).

Author contributions

MI designed the study, performed the analyses, and prepared all figures. MI wrote the initial draft of the manuscript. MI and TO contributed to the interpretation of the results. All authors contributed to improving the manuscript.

Acknowledgements:

Jonathan D. Sharp and the reviewers are acknowledged for providing comments that prompted

significant improvements to this manuscript.

Financial support:

This research has been supported by the Institute for Basic Science (grant no. IBS-R028-D1) and the Japan Society for the Promotion of Science (JSPS) through a Grant-in-Aid for Scientific Research JP22H00176.

Figure captions:

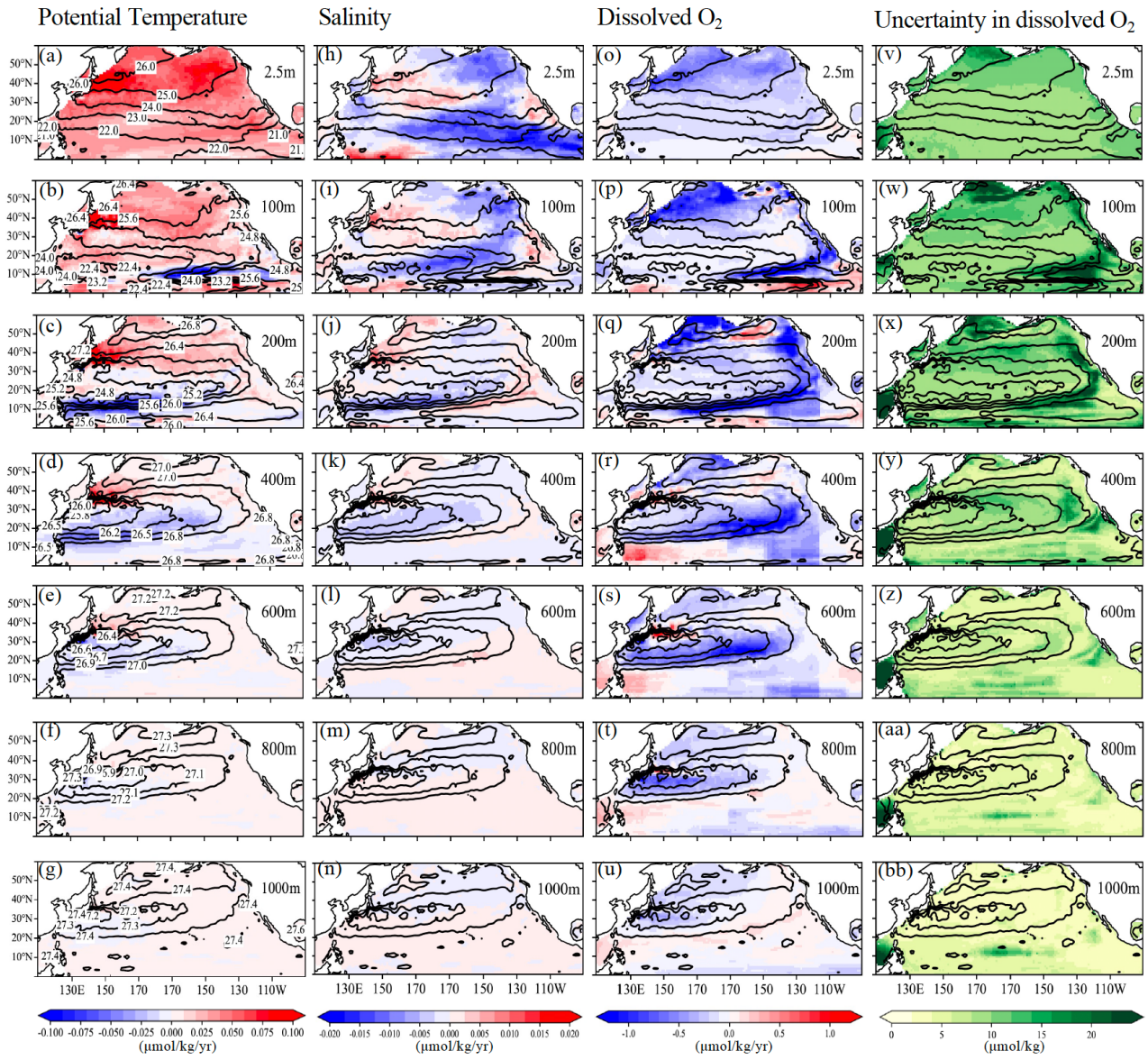

556

557 **Figure 1** Horizontal distributions of linear trends (μmol/kg/yr) in (a–g) potential temperature, (h–n)
558 salinity, and (o–u) dissolved oxygen (O_2) during the observational period at depths of 0, 100, 200,
559 400, 600, 800, and 1000 m, respectively. Contours denote potential density at each depth. Labels for
560 the potential density are shown only in the potential temperature sections. Corresponding distributions
561 of the mean uncertainty in dissolved O_2 (μmol/kg) are presented in panels (v–bb).

562

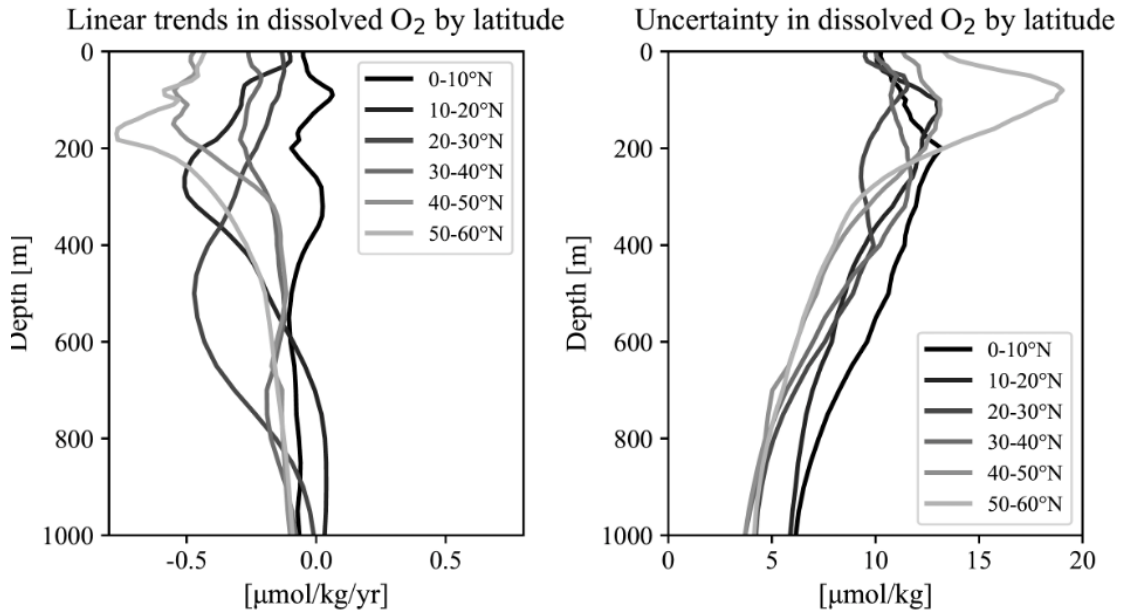

563

564 **Figure 2** Vertical profiles of linear trends and uncertainty in dissolved O_2 by latitude.

565

566

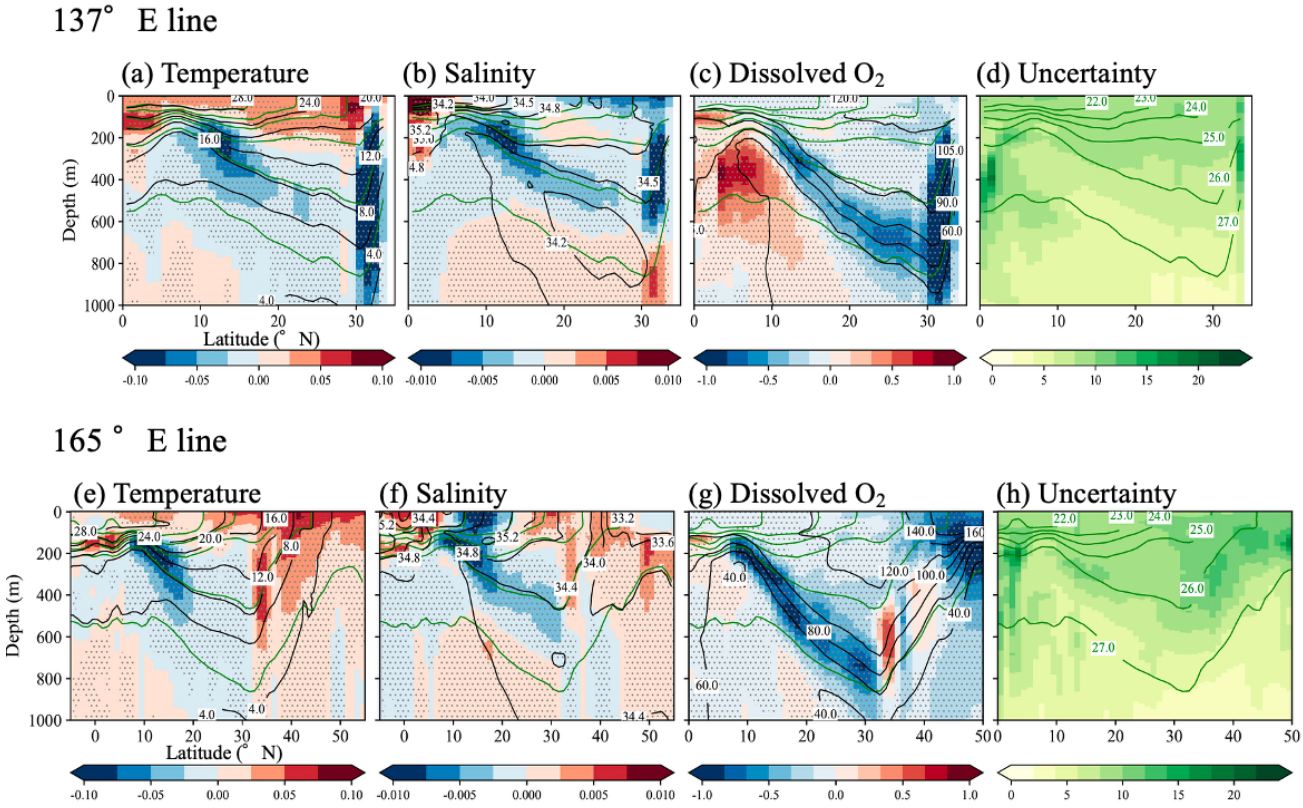

567

568 **Figure 3** Vertical sections showing linear trends in potential temperature (a, e), salinity (b, f), and

dissolved O_2 (c, g) along the 137°E and 165°E meridians, respectively. Corresponding vertical sections of the mean uncertainty are presented in panels (d) and (h). Black contour lines indicate the mean potential temperature (a, e), salinity (b, f), and dissolved oxygen (c, g) over the period 2004–2023, while green contour lines represent the mean potential density. Labels for the potential density are shown only in the uncertainty sections.

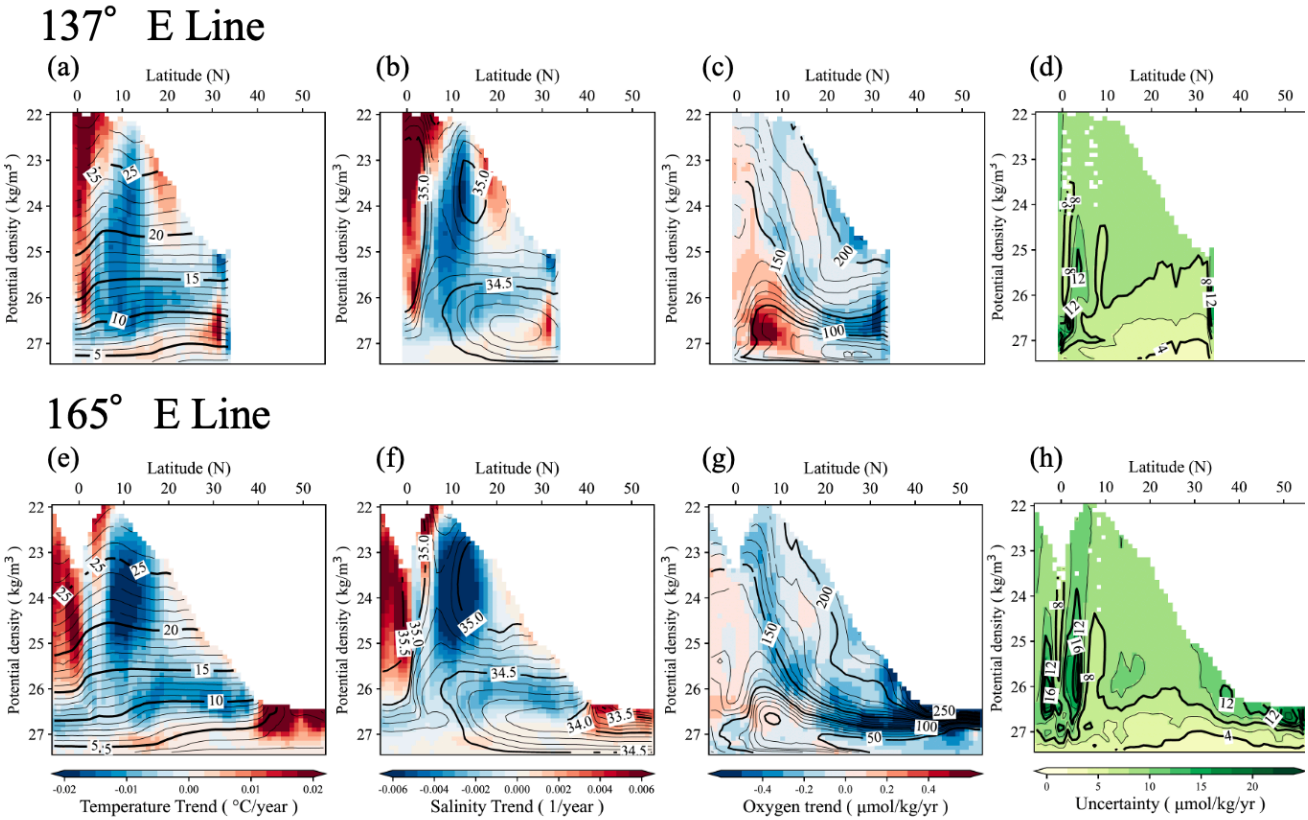

Figure 4 Linear trends in (a, e) potential temperature, (b, f) salinity, (c, g), and dissolved O_2 on each isopycnal surface at intervals of $0.1\sigma_\theta$, calculated at every 1.0 deg of latitude in 137 °E and 165 °E lines, respectively. Contour lines represent the mean values during the target observation periods, plotted at intervals of $0.1\sigma_\theta$ for each 1 deg. of latitude. Fig. 4 (d) and 4 (h) are the same but show the averaged uncertainty during the target observation periods, on each isopycnal surface.

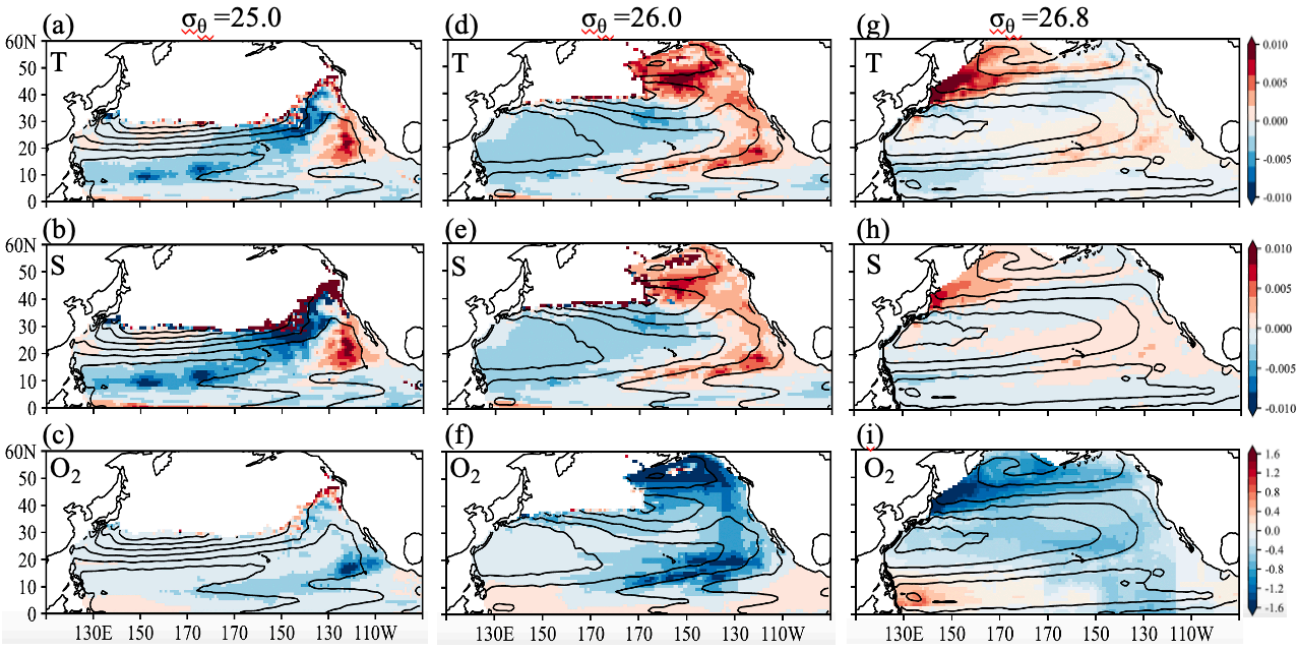

Figure 5 Linear trends in (a) potential temperature, (b) salinity, and (c) dissolved O_2 on each isopycnal surface at 25.0, 26.0, and 26.8σ_θ. Contour lines represent geostrophic flow streamlines on 26.0 and 26.8σ_θ surfaces, relative to 2000 m.

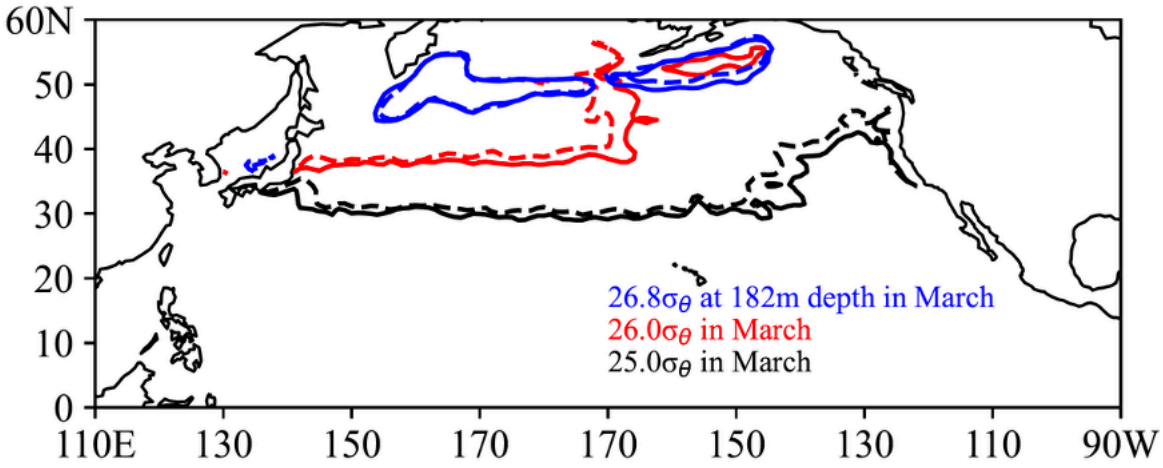

Figure 6 Density contours of 25.0σ_θ (black), 26.0σ_θ (red), and 26.8σ_θ (blue). Solid lines indicate the average density contours for March 2004–2009, while dashed lines represent 2019–2023.

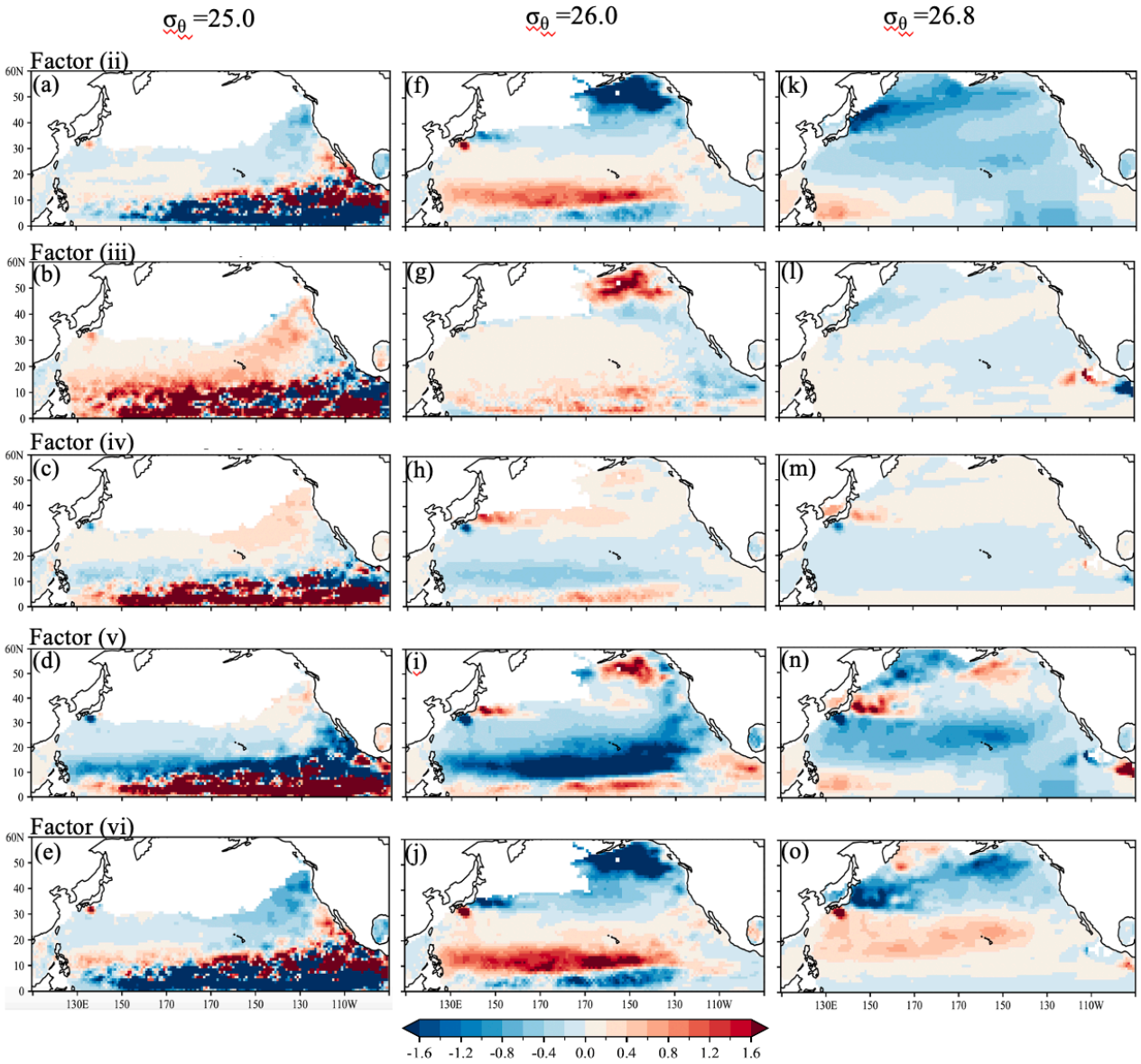

592

593 **Figure 7** Horizontal distributions of the magnitude of each factor contributing to the rate of O_2 change
594 on 25.0, 26.0, and 26.8 σ_θ in Eq. (1). The rate of O_2 change on each isopycnal surface is decomposed
595 into the following components: (ii) the apparent contribution from vertical heave (deepening or
596 shoaling) of isopycnal surfaces associated with warming and/or surface freshening; (iii) the
597 contribution from changes in oxygen solubility (O_2^{sat}) associated with temperature and salinity
598 variations; (iv) the contribution from vertical heave acting on the background solubility gradient;
599 (v) the contribution from net changes in apparent oxygen utilization (AOU) associated with air–sea
600 disequilibrium, biological activity, and lateral advection and/or circulation; and (vi) the contribution
601 from vertical heave acting on AOU gradients, independent of solubility changes. This decomposition
602 is applied to the reconstructed dissolved oxygen fields obtained from linear regression analysis.

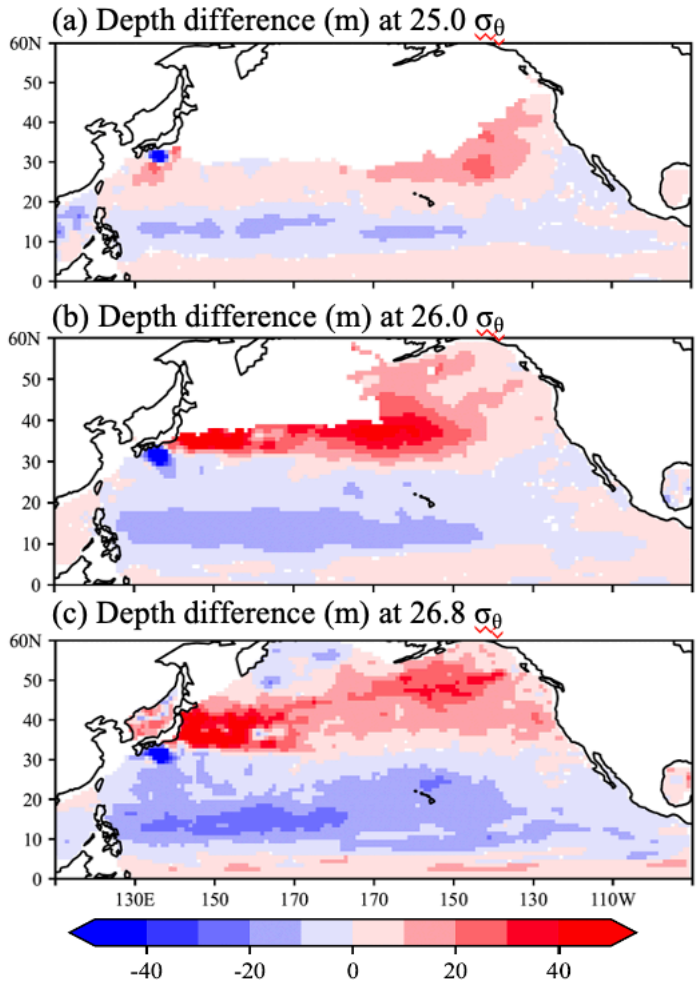

Figure 8 Depth difference (m) between the 5-year averaged data in March, 2004–2009 and 2018–2023 at 25.0, 26.0, and 26.8σ_θ. The reconstructed O_2 data estimated from the linear regression analysis were used in this calculation. Positive and negative values indicate the deepening and shallowing, respectively, from the depth of each density in 2004– 2023.

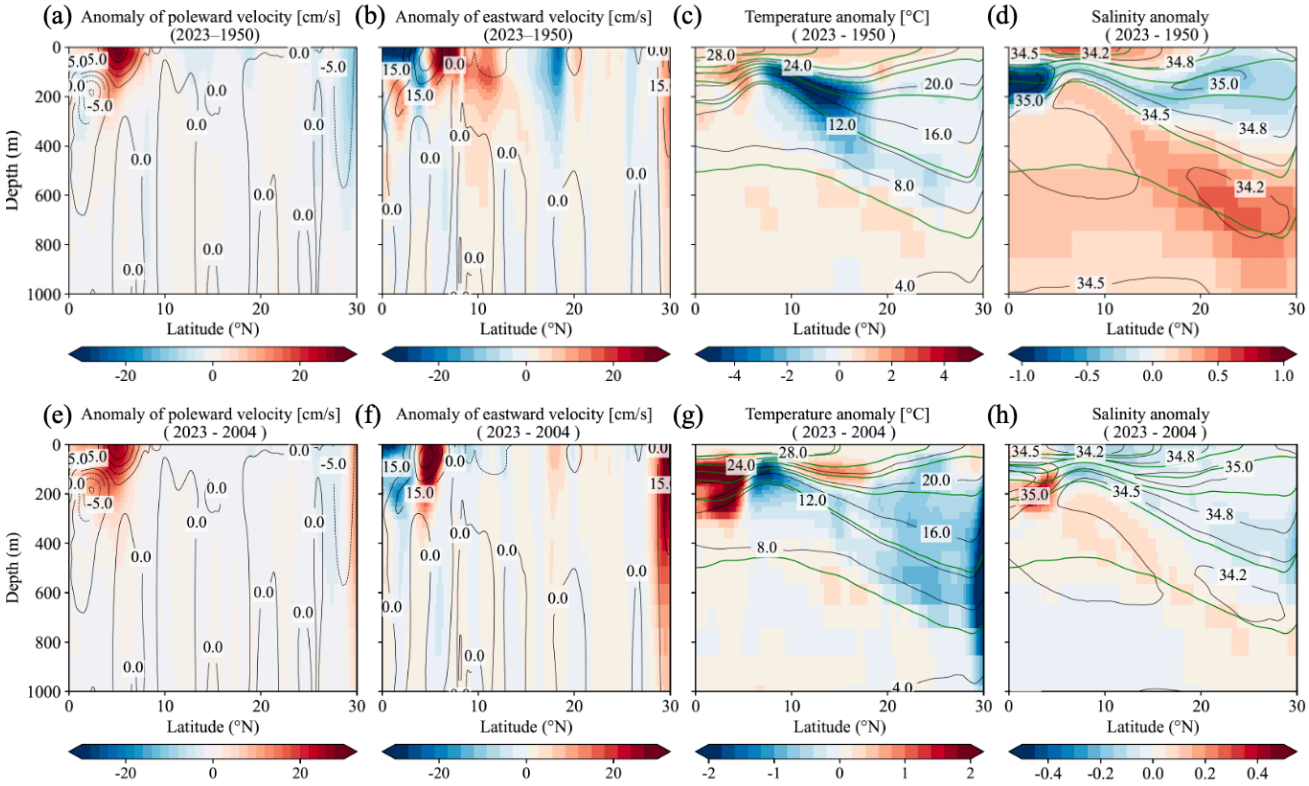

610

611 **Figure 9.** Anomaly of poleward and eastward velocity, potential temperature, and salinity in the OFES
612 model outputs from 1950 to 2023 (a–d) and from 2004 to 2023 (e–h), respectively, in the 137°E line.
613 Contours of averaged values of poleward and eastward velocity, potential temperature, and salinity
614 during the target period are also shown in each figure. Green contour lines in (c–d, g–h) indicate the
615 average potential density of 22, 23, 24, 25, 26, and 27σ_θ, during the target periods.

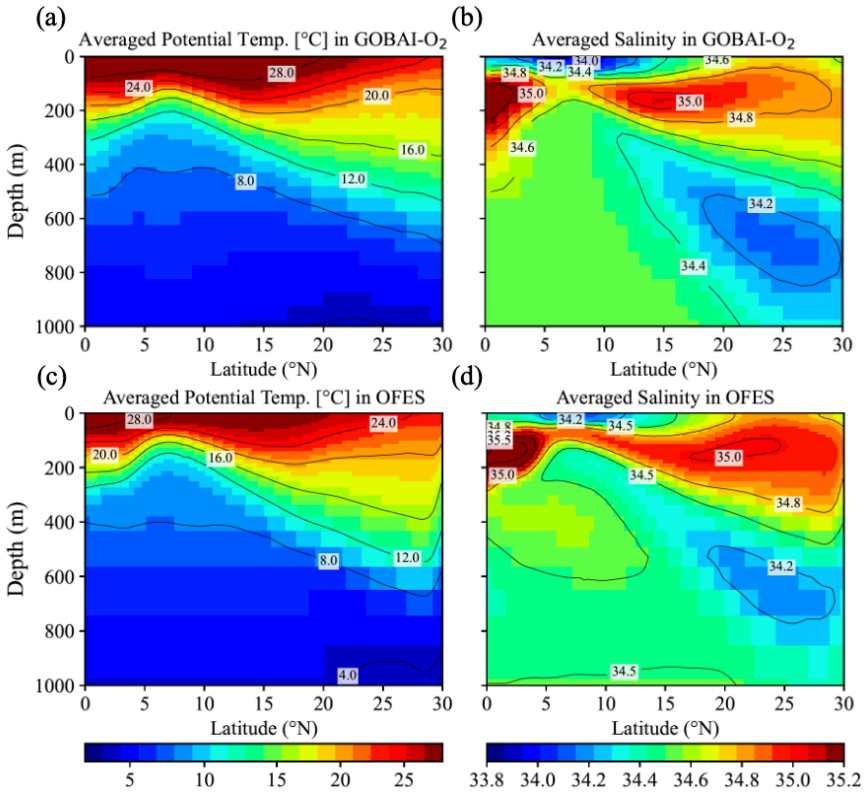

616

617 **Figure 10.** Averaged Potential Temperature (a, c) and salinity (b, d) in GOBAI-O_2 from 2004 to
618 2023 and OFES data from 1950 to 2023, respectively, in the 137°E line.

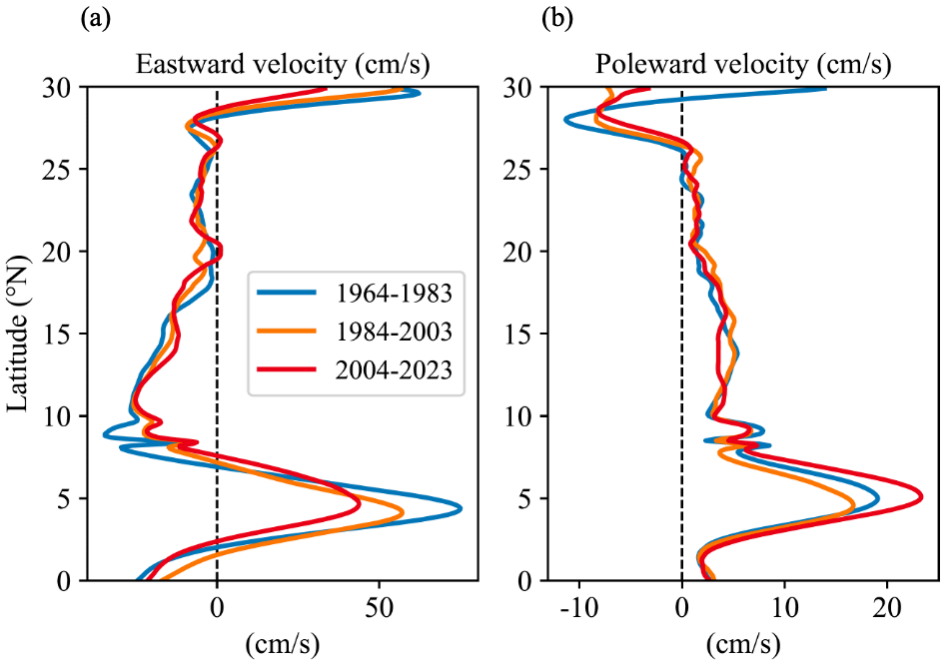

619

620 **Figure 11.** Latitudinal distribution of averaged eastward (a) and poleward velocity (b) in the OFES
621 data from 1964 to 1983, from 1984 to 2003, and from 2004 to 2023, respectively, in the 137°E line.

622

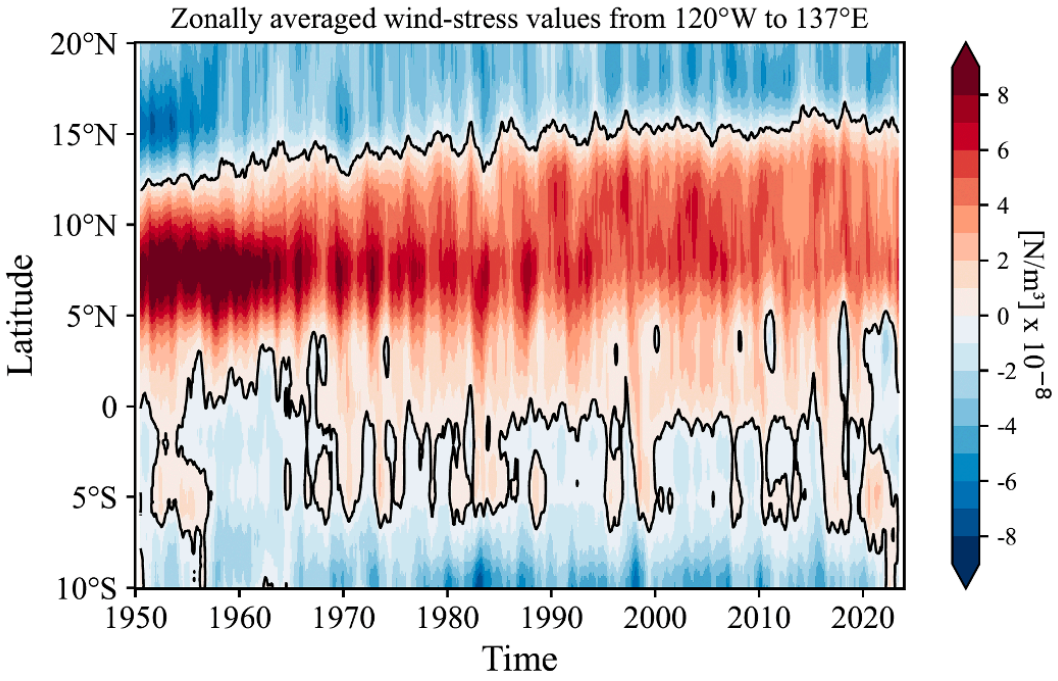

623

624 **Figure 12.** NCEP-NCAR wind-stress curl values zonally averaged from 137°E to 120° W from 1950
625 to 2023. A 13-month running-mean filter has been applied in time.

626

627 **Appendix: Essential concepts and derivations for Equation (2–3)**

628 The essential concepts and derivations for equations (2) and (3) were originally proposed by Takatani
629 et al. [2012] and subsequently described in detail by Sasano et al. [2015]. Here, we briefly summarize
630 and follow their derivation.

631

632 When the temperature at a depth z_A increases from θ_A to θ_A' as a result of increased ocean heat
633 content, the density at that depth decreases from σ_A to σ_A'. For simplicity, the vertical salinity profile
634 is assumed to remain unchanged with time. As a consequence, the isopycnal surface of σ_A deepens
635 from z_A to z_B (Figure S5). If surface freshening occurs simultaneously due to a net freshwater input,
636 both the density decreases at z_A (from σ_A to σ_A') and the deepening of the isopycnal surface (from
637 z_A to z_B) are enhanced. Because density is a function of temperature and salinity ($\sigma = f(\theta, S)$), the

638 density of the isopycnal surface σ_A can be expressed as

639 $$\sigma_A = f(\theta_A, S_A) \quad \text{(before warming)} \quad \text{(C1)}$$

640 $$= f(\theta_B', S_B). \quad \text{(after warming)} \quad \text{(C2)}$$

641 Here, S_A and S_B denote salinity at depth z_A and z_B, respectively, and θ_B' represents the temperature at
642 density σ_A at depth z_B after warming. The depth z_B is determined by satisfying Eqs. (C1) and (C2).
643 In the region where salinity decreases with depth (e.g., above the salinity minimum layer of NPIW),
644 $S_A > S_B$, and therefore $\theta_A > \theta_B'$. This implies that the potential temperature on an isopycnal surface
645 effectively decreases as a consequence of warming, and that biogeochemical properties on the same
646 isopycnal surface are also expected to change.

647

648 For a tracer X whose vertical profile with respect to depth does not change with time (e.g., salinity;
649 see Figure S5 (c)), the temporal change of X on the potential density surface σ_A is attributed solely
650 to the apparent change caused by the deepening of the isopycnal surface from z_A to z_B:

651 $$\frac{\partial X}{\partial t} = \left(\frac{\partial X}{\partial z} \cdot \frac{\partial z}{\partial t}\right) \quad \text{(C3)}$$

652 Here, $\partial X/\partial t$ represents the temporal change of X observed on σ_A (gray arrows in Figure S5), z
653 denotes the depth of σ_A, $\partial X/\partial z$ is the vertical gradient of X with respect to the depth (assumed to be
654 time-invariant), and $\partial z/\partial t$ is the rate of deepening of the isopycnal surface σ_A. The product
655 $\partial X/\partial z \cdot \partial z/\partial t$ represents the effect of isopycnal deepening (white arrows in Figure S5),
656 corresponding to the difference between the filled square and filled circle.

657

658 For a variable Y whose vertical profile evolves with time while warming occurs simultaneously, the
659 temporal change of Y on the density surface σ_A can be expressed as the sum of two components: the
660 contribution due to the isopycnal deepening from z_A to z_B and the net temporal change of Y,

661 ($\partial Y/\partial t$)$_{net}$ between the time before and after warming:

662 $$\frac{\partial Y}{\partial t} = \left(\frac{\partial Y}{\partial z} \cdot \frac{\partial z}{\partial t}\right) + \left(\frac{\partial Y}{\partial t}\right)_{net} \qquad (C4)$$

663 To evaluate the net change ($\partial Y/\partial z$)$_{net}$ (illustrated by the blue arrows of a difference in symbols
664 between filled square and open square in Figure S5), it is necessary to evaluate the contribution of the
665 temporal change of *Y* due to the isopycnal deepening and to subtract it from the change of *Y* observed
666 at density σ_A. For instance, the change of O_2^{sat} in Figure S5 (f) is observed along the gray isopycnal
667 surface (large white arrow), whereas the net change (large blue and pink arrows) is obtained as the
668 difference between the observed change and the deepening effect.

669

670 The dissolved oxygen concentration O_2 can be expressed as:

671 $$O_2 = O_2^{sat} - AOU, \qquad (C5)$$

672 where O_2^{sat} is the oxygen saturation concentration (a function of temperature and salinity), and AOU
673 is "apparent oxygen utilization", representing the oxygen consumed by biological processes since
674 subduction. Near the surface, AOU is typically small, and its contributions can be neglected.

675

676 Following Eq. (C4), the temporal change of O_2 on a given isopycnal surface at a fixed station is:

677 $$\frac{\partial O_2}{\partial t} = \left(\frac{\partial O_2}{\partial z} \cdot \frac{\partial z}{\partial t}\right) + \left(\frac{\partial O_2}{\partial t}\right)_{net}. \qquad (C6)$$

678 Similarly,

679 $$\frac{\partial O_2^{sat}}{\partial t} = \left(\frac{\partial O_2^{sat}}{\partial z} \cdot \frac{\partial z}{\partial t}\right) + \left(\frac{\partial O_2^{sat}}{\partial t}\right)_{net}, \qquad (C7)$$

680 and

681 $$\frac{\partial AOU}{\partial t} = \left(\frac{\partial (AOU)}{\partial z} \cdot \frac{\partial z}{\partial t}\right) + \left(\frac{\partial (AOU)}{\partial t}\right)_{net}. \qquad (C8)$$

682 The term $(\partial O_2^{sat}/\partial t)_{\text{net}}$ is directly related to warming, because O_2^{sat} depends on temperature and
683 salinity. If AOU does not change with time, that is, if changes in O_2 arise solely from changes in O_2^{sat},
684 then $\partial(AOU)/\partial t$ follows Eq. (C3) and $(\partial(AOU)/\partial t)_{net} = 0$. If AOU varies with time, however,
685 $\partial(AOU)/\partial t$ follows Eq. (C4) and $(\partial(AOU)/\partial t)_{net} \neq 0$, as illustrated by the dashed gray line in
686 Figure S5 (g).

687

688 Because O_2 is defined by Eq. (C5), the net temporal change of O_2 on an isopycnal surface is

689 $$\left(\frac{\partial O_2}{\partial t}\right)_{net} = \left(\frac{\partial O_2^{sat}}{\partial t}\right)_{net} - \left(\frac{\partial (AOU)}{\partial t}\right)_{net}. \qquad \text{(C9)}$$

690 Combining Eqs. (C6) and (C9), the total temporal change of O_2 on an isopycnal surface can be
691 written as

692 $$\left(\frac{\partial O_2}{\partial t}\right) = \left(\frac{\partial O_2}{\partial z}\cdot\frac{\partial z}{\partial t}\right) + \left(\frac{\partial O_2^{sat}}{\partial t}\right)_{net} - \left(\frac{\partial (AOU)}{\partial t}\right)_{net}, \qquad \text{(C10)}$$

693 which corresponds to Eq. (1) in the main text. Eq. (C10) corresponds to an arrow in Figure S5 (e),
694 represented from left to right by the large gray arrow, white, blue, and pink arrows. The large blue
695 arrow is identical to Figure S5 (f), while the large pink arrow corresponds to Figure S5(g), but with
696 its direction reversed. Finally, substituting Eqs. (C7) and (C8) into (C10)

697 $$\underbrace{\frac{\partial O_2}{\partial t}}_{\text{(i)}} = \underbrace{\left(\frac{\partial O_2}{\partial z}\frac{\partial z}{\partial t}\right)}_{\text{(ii)}} + \underbrace{\left(\frac{\partial O_2^{sat}}{\partial t} - \frac{\partial O_2^{sat}}{\partial z}\frac{\partial z}{\partial t}\right)}_{\text{(iii)}} - \underbrace{\left(\frac{\partial (AOU)}{\partial t} - \frac{\partial (AOU)}{\partial z}\frac{\partial z}{\partial t}\right)}_{\text{(iv)}\quad\text{(v)}\quad\text{(vi)}}, \quad \text{(C11)}$$

698 (i) (ii) (iii) (iv) (v) (vi)

699 which corresponds to Eq. (2) in the main text. Note: The signs in terms (v) and (vi) in Eq. (3) are
700 reversed relative to those in Eq. (C11) for convenience.

701

702 Table A1 The physical interpretation of each term in the oxygen tendency decomposition shown in Eq. (3) and
703 Eq. (C11) is summarized.

Term	Mathematical form	Physical interpretation
(ii)	$(\partial O_2/\partial z)(\partial z/\partial t)$	Vertical heave acting on the O_2 gradient
(iii)	$\partial O_2^{sat}/\partial t$	Solubility effect due to temperature and salinity changes
(iv)	$-(\partial O_2^{sat}/\partial z)(\partial z/\partial t)$	Vertical heave acting on the solubility gradient
(v)	$\partial AOU/\partial t$	AOU changes related to air–sea disequilibrium, biological activity and lateral circulation
(vi)	$-(\partial AOU/\partial z)(\partial z/\partial t)$	Vertical heave of the AOU gradient

704

705

706 **Data availability:**

707 GOBAI-O_2 [Sharp et al. 2022; 2023] can be accessed from NOAA's National Centers for
708 Environmental Information at https://accession.nodc.noaa.gov/0259304 (doi: 10.25921/z72m-yz67).

709

710 **References:**

711 Alkire, M. B., D'Asaro, E., Lee, C., Jane Perry, M., Gray, A., Cetinić, I., et al. (2012). Estimates of
712 net community production and export using high-resolution, Lagrangian measurements of O2, NO3−,
713 and POC through the evolution of a spring diatom bloom in the North Atlantic. *Deep Sea Research*
714 *Part I: Oceanographic Research Papers*, *64*, 157–174. https://doi.org/10.1016/j.dsr.2012.01.012

715 Berman-Frank, I., Lundgren, P., & Falkowski, P. (2003). Nitrogen fixation and photosynthetic oxygen
716 evolution in cyanobacteria. *Research in Microbiology*, *154*(3), 157–164.
717 https://doi.org/10.1016/S0923-2508(03)00029-9

718 Bittig, H. C., Fiedler, B., Scholz, R., Krahmann, G., & Körtzinger, A. (2014). Time response of oxygen
719 optodes on profiling platforms and its dependence on flow speed and temperature. *Limnology and*
720 *Oceanography: Methods*, *12*(8), 617–636. https://doi.org/10.4319/lom.2014.12.617

721 Bittig, H. C., & Körtzinger, A. (2015). Tackling Oxygen Optode Drift: Near-Surface and In-Air
722 Oxygen Optode Measurements on a Float Provide an Accurate in Situ Reference.
723 https://doi.org/10.1175/JTECH-D-14-00162.1
724 Bittig, H. C., Körtzinger, A., Neill, C., van Ooijen, E., Plant, J. N., Hahn, J., et al. (2018a). Oxygen
725 Optode Sensors: Principle, Characterization, Calibration, and Application in the Ocean. *Frontiers in*
726 *Marine Science*, *4*. https://doi.org/10.3389/fmars.2017.00429
727 Bittig, H. C., Steinhoff, T., Claustre, H., Fiedler, B., Williams, N. L., Sauzède, R., et al. (2018b). An
728 Alternative to Static Climatologies: Robust Estimation of Open Ocean CO_2 Variables and Nutrient
729 Concentrations From T, S, and O_2 Data Using Bayesian Neural Networks. *Frontiers in Marine*
730 *Science*, *5*. https://doi.org/10.3389/fmars.2018.00328
731 Bopp, L., Resplandy, L., Orr, J. C., Doney, S. C., Dunne, J. P., Gehlen, M., et al. (2013). Multiple
732 stressors of ocean ecosystems in the 21st century: projections with CMIP5 models. *Biogeosciences*,
733 *10*(10), 6225–6245. https://doi.org/10.5194/bg-10-6225-2013
734 Boyer, T. P., and S. Levitus (1997), Objective Analyses of Temperature and Salinity for the World
735 Ocean on a 1/48 Grid, vol. 11, NOAA Atlas NESDIS, Natl. Oceanic and Atmos. Admin., Silver Spring,
736 Md.
737 Boyer, T. P., Antonov, J. I., Baranova, O. K., Coleman, C., Garcia, H. E., Grodsky, A., et al. (2013).
738 World Ocean Database 2013. Retrieved from
739 https://repository.oceanbestpractices.org/handle/11329/357
740 Breiman, L. (2001). Random Forests. *Machine Learning*, *45*(1), 5–32.
741 https://doi.org/10.1023/A:1010933404324
742 Breitburg, D., Levin, L. A., Oschlies, A., Grégoire, M., Chavez, F. P., Conley, D. J., et al. (2018).
743 Declining oxygen in the global ocean and coastal waters. *Science*, *359*(6371), eaam7240.
744 https://doi.org/10.1126/science.aam7240

745 Bushinsky, S. M., Emerson, S. R., Riser, S. C., & Swift, D. D. (2016). Accurate oxygen measurements
746 on modified Argo floats using in situ air calibrations. *Limnology and Oceanography: Methods*, *14*(8),
747 491–505. https://doi.org/10.1002/lom3.10107
748 Bushinsky, S.M., Nachod, Z., Fassbender, A.J., Tamsitt, V., Takeshita, Y., Williams, N., 2025. Offset
749 Between Profiling Float and Shipboard Oxygen Observations at Depth Imparts Bias on Float pH and
750 Derived pCO2. Global Biogeochemical Cycles 39, e2024GB008185.
751 https://doi.org/10.1029/2024GB008185
752 Chen, X., Qiu, B., Du, Y., Chen, S., & Qi, Y. (2016). Interannual and interdecadal variability of the
753 North Equatorial Countercurrent in the Western Pacific. *Journal of Geophysical Research: Oceans*,
754 *121*(10), 7743–7758. https://doi.org/10.1002/2016JC012190
755 Claustre, H., Johnson, K. S., & Takeshita, Y. (2020). Observing the Global Ocean with
756 Biogeochemical-Argo. *Annual Review of Marine Science*, *12*(Volume 12, 2020), 23–48.
757 https://doi.org/10.1146/annurev-marine-010419-010956
758 D'Asaro, E. A., & McNeil, C. (2013). Calibration and Stability of Oxygen Sensors on Autonomous
759 Floats. https://doi.org/10.1175/JTECH-D-12-00222.1
760 Drucker, R., & Riser, S. C. (2016). In situ phase-domain calibration of oxygen Optodes on profiling
761 floats. *Methods in Oceanography*, *17*, 296–318. https://doi.org/10.1016/j.mio.2016.09.007
762 Estapa, M. L., Feen, M. L., & Breves, E. (2019). Direct Observations of Biological Carbon Export
763 From Profiling Floats in the Subtropical North Atlantic. *Global Biogeochemical Cycles*, *33*(3), 282–
764 300. https://doi.org/10.1029/2018GB006098
765 Giglio, D., Lyubchich, V., & Mazloff, M. R. (2018). Estimating Oxygen in the Southern Ocean Using
766 Argo Temperature and Salinity. *Journal of Geophysical Research: Oceans*, *123*(6), 4280–4297.
767 https://doi.org/10.1029/2017JC013404
768 Helm, K. P., Bindoff, N. L., & Church, J. A. (2011). Observed decreases in oxygen content of the
769 global ocean. *Geophysical Research Letters*, *38*(23). https://doi.org/10.1029/2011GL049513

Ito, T., Minobe, S., Long, M. C., & Deutsch, C. (2017). Upper ocean O_2 trends: 1958–2015. *Geophysical Research Letters*, *44*(9), 4214–4223. https://doi.org/10.1002/2017GL073613

Ito, T., Cervania, A., Cross, K., Ainchwar, S., & Delawalla, S. (2024). Mapping Dissolved Oxygen Concentrations by Combining Shipboard and Argo Observations Using Machine Learning Algorithms. *Journal of Geophysical Research: Machine Learning and Computation*, *1*(3), e2024JH000272. https://doi.org/10.1029/2024JH000272

Johnson, K. S., Plant, J. N., Riser, S. C., & Gilbert, D. (2015). Air Oxygen Calibration of Oxygen Optodes on a Profiling Float Array. https://doi.org/10.1175/JTECH-D-15-0101.1

Johnson, K. S., Plant, J. N., Coletti, L. J., Jannasch, H. W., Sakamoto, C. M., Riser, S. C., et al. (2017). Biogeochemical sensor performance in the SOCCOM profiling float array. *Journal of Geophysical Research: Oceans*, *122*(8), 6416–6436. https://doi.org/10.1002/2017JC012838

Johnson, K. S., & Bif, M. B. (2021). Constraint on net primary productivity of the global ocean by Argo oxygen measurements. *Nature Geoscience*, *14*(10), 769–774. https://doi.org/10.1038/s41561-021-00807-z

Kalnay, E., Kanamitsu, M., Kistler, R., Collins, W., Deaven, D., Gandin, L., et al. (1996). The NCEP/NCAR 40-Year Reanalysis Project. Retrieved from https://journals.ametsoc.org/view/journals/bams/77/3/1520-0477_1996_077_0437_tnyrp_2_0_co_2.xml

Kara, A. B., Rochford, P. A., & Hurlburt, H. E. (2000). An optimal definition for ocean mixed layer depth. *Journal of Geophysical Research: Oceans*, *105*(C7), 16803–16821. https://doi.org/10.1029/2000JC900072

Keeling, R. F., Körtzinger, A., & Gruber, N. (2010). Ocean Deoxygenation in a Warming World. *Annual Review of Marine Science*, *2* (Volume 2, 2010), 199–229. https://doi.org/10.1146/annurev.marine.010908.163855

794 Kolodziejczyk, N., Portela, E., Thierry, V., & Prigent, A. (2024). ISASO2: recent trends and regional
795 patterns of ocean dissolved oxygen change. *Earth System Science Data*, *16*(11), 5191–5206.
796 https://doi.org/10.5194/essd-16-5191-2024
797 Körtzinger, A., Schimanski, J., & Send, U. (2005). High Quality Oxygen Measurements from Profiling
798 Floats: A Promising New Technique. https://doi.org/10.1175/JTECH1701.1
799 Kwiatkowski, L., Torres, O., Bopp, L., Aumont, O., Chamberlain, M., Christian, J. R., et al. (2020).
800 Twenty-first century ocean warming, acidification, deoxygenation, and upper-ocean nutrient and
801 primary production decline from CMIP6 model projections. *Biogeosciences*, *17*(13), 3439–3470.
802 https://doi.org/10.5194/bg-17-3439-2020
803 Lauvset, S. K., Lange, N., Tanhua, T., Bittig, H. C., Olsen, A., Kozyr, A., et al. (2022b).
804 GLODAPv2.2022: the latest version of the global interior ocean biogeochemical data product. *Earth*
805 *System Science Data*, *14*(12), 5543–5572. https://doi.org/10.5194/essd-14-5543-2022
806 Li, C., Huang, Jianping, Ding, L., Liu, X., Yu, H., Huang, Jiping, 2020. Increasing Escape of Oxygen
807 From Oceans Under Climate Change. Geophysical Research Letters 47, e2019GL086345.
808 https://doi.org/10.1029/2019GL086345
809 Limburg, K. E., Breitburg, D., Swaney, D. P., & Jacinto, G. (2020). Ocean Deoxygenation: A Primer.
810 *One Earth*, *2*(1), 24–29. https://doi.org/10.1016/j.oneear.2020.01.001
811 Masumoto, Y., Sasaki, H., Kagimoto, T., Komori, N., Ishida, A., Sasai, Y., et al. (2004). A fifty-year
812 eddy-resolving simulation of the world ocean: Preliminary outcomes of OFES (OGCM for the Earth
813 Simulator). Journal of the Earth Simulator, 1,35–56. https://www.jamstec.
814 go.jp/ceist/j/publication/journal/jes_vol.1/pdf/JES1-3.2-masumoto.pdf
815 Masumoto, Y. (2010). Sharing the results of a high-resolution ocean general circulation model under
816 a multi-discipline framework—a review of OFES activities. *Ocean Dynamics*, *60*(3), 633–652.
817 https://doi.org/10.1007/s10236-010-0297-z

Maurer, T. L., Plant, J. N., & Johnson, K. S. (2021). Delayed-Mode Quality Control of Oxygen, Nitrate, and pH Data on SOCCOM Biogeochemical Profiling Floats. *Frontiers in Marine Science*, *8*. https://doi.org/10.3389/fmars.2021.683207

Nakamura, T., & Awaji, T. (2004). Tidally induced diapycnal mixing in the Kuril Straits and its role in water transformation and transport: A three-dimensional nonhydrostatic model experiment. *Journal of Geophysical Research: Oceans*, *109*(C9). https://doi.org/10.1029/2003JC001850

Nakamura, T., Awaji, T., Hatayama, T., Akitomo, K., Takizawa, T., Kono, T., et al. (2000a). The Generation of Large-Amplitude Unsteady Lee Waves by Subinertial K1 Tidal Flow: A Possible Vertical Mixing Mechanism in the Kuril Straits. Retrieved from https://journals.ametsoc.org/view/journals/phoc/30/7/1520-0485_2000_030_1601_tgolau_2.0.co_2.xml

Nakamura, T., Awaji, T., Hatayama, T., Akitomo, K., & Takizawa, T. (2000b). Tidal Exchange through the Kuril Straits. Retrieved from https://journals.ametsoc.org/view/journals/phoc/30/7/1520-0485_2000_030_1622_tettks_2.0.co_2.xml

Nicholson, D. P., & Feen, M. L. (2017). Air calibration of an oxygen optode on an underwater glider. *Limnology and Oceanography: Methods*, *15*(5), 495–502. https://doi.org/10.1002/lom3.10177

Ogata, T., & Nonaka, M. (2020). Mechanisms of Long-Term Variability and Recent Trend of Salinity Along 137°E. *Journal of Geophysical Research: Oceans*, *125*(2), e2019JC015290. https://doi.org/10.1029/2019JC015290

Pacanowski, R. C., and S. M. Griffies (2000), MOM 3.0 Manual, Technical Report 4, 680 pp., Geophys. Fluid Dyn. Lab., Princeton, N. J. Philander, S. G. H. (1990), El Niño, La Niiña, and the Southern Oscillation, pp. 293, Academic Press, San Diego, Calif.

Pörtner, H. O., & Farrell, A. P. (2008). Physiology and Climate Change. *Science*, *322*(5902), 690–692. https://doi.org/10.1126/science.1163156

842 Pozo Buil, M., & Di Lorenzo, E. (2017). Decadal dynamics and predictability of oxygen and
843 subsurface tracers in the California Current System. *Geophysical Research Letters*, *44*(9), 4204–4213.
844 https://doi.org/10.1002/2017GL072931
845 Reid, J. L. (1997). On the total geostrophic circulation of the pacific ocean: flow patterns, tracers, and
846 transports. *Progress in Oceanography*, *39*(4), 263–352. https://doi.org/10.1016/S0079-
847 6611(97)00012-8
848 Roemmich, D., & Gilson, J. (2009). The 2004–2008 mean and annual cycle of temperature, salinity,
849 and steric height in the global ocean from the Argo Program. *Progress in Oceanography*, *82*(2), 81–
850 100. https://doi.org/10.1016/j.pocean.2009.03.004
851 Sampaio, E., Santos, C., Rosa, I. C., Ferreira, V., Pörtner, H.-O., Duarte, C. M., et al. (2021). Impacts
852 of hypoxic events surpass those of future ocean warming and acidification. *Nature Ecology &*
853 *Evolution*, *5*(3), 311–321. https://doi.org/10.1038/s41559-020-01370-3
854 Sasaki, H., Nonaka, M., Masumoto, Y., Sasai, Y., Uehara, H., & Sakuma, H. (2008). An Eddy-
855 Resolving Hindcast Simulation of the Quasiglobal Ocean from 1950 to 2003 on the Earth Simulator.
856 In K. Hamilton & W. Ohfuchi (Eds.), *High Resolution Numerical Modelling of the Atmosphere and*
857 *Ocean* (pp. 157–185). New York, NY: Springer. https://doi.org/10.1007/978-0-387-49791-4_10
858 Sasano, D., Takatani, Y., Kosugi, N., Nakano, T., Midorikawa, T., & Ishii, M. (2015). Multidecadal
859 trends of oxygen and their controlling factors in the western North Pacific. *Global Biogeochemical*
860 *Cycles*, *29*(7), 935–956. https://doi.org/10.1002/2014GB005065
861 Sasano, D., Takatani, Y., Kosugi, N., Nakano, T., Midorikawa, T., & Ishii, M. (2018). Decline and
862 Bidecadal Oscillations of Dissolved Oxygen in the Oyashio Region and Their Propagation to the
863 Western North Pacific. *Global Biogeochemical Cycles*, *32*(6), 909–931.
864 https://doi.org/10.1029/2017GB005876
865 Schmidtko, S., Stramma, L., & Visbeck, M. (2017). Decline in global oceanic oxygen content during
866 the past five decades. *Nature*, *542*(7641), 335–339. https://doi.org/10.1038/nature21399

Sharp, J. D., Fassbender, A. J., Carter, B. R., Johnson, G. C., Schultz, C., Dunne, J. P. (2022). GOBAI-O_2: A Global Gridded Monthly Dataset of Ocean Interior Dissolved Oxygen Concentrations Based on Shipboard and Autonomous Observations (NCEI Accession 0259304). NOAA National Centers for Environmental Information. Dataset. https://doi.org/10.25921/z72m-yz67.

Sharp, J. D., Fassbender, A. J., Carter, B. R., Johnson, G. C., Schultz, C., & Dunne, J. P. (2023). GOBAI-O_2: temporally and spatially resolved fields of ocean interior dissolved oxygen over nearly 2 decades. *Earth System Science Data*, *15*(10), 4481–4518. https://doi.org/10.5194/essd-15-4481-2023

Stramma, L., Johnson, G. C., Sprintall, J., & Mohrholz, V. (2008). Expanding Oxygen-Minimum Zones in the Tropical Oceans. *Science*, *320*(5876), 655–658. https://doi.org/10.1126/science.1153847

Stramma, L., Schmidtko, S., Bograd, S. J., Ono, T., Ross, T., Sasano, D., & Whitney, F. A. (2020). Trends and decadal oscillations of oxygen and nutrients at 50 to 300 m depth in the equatorial and North Pacific. *Biogeosciences*, *17*(3), 813–831. https://doi.org/10.5194/bg-17-813-2020

Stramma, L., & Schmidtko, S. (2021). Tropical deoxygenation sites revisited to investigate oxygen and nutrient trends. *Ocean Science*, *17*(3), 833–847. https://doi.org/10.5194/os-17-833-2021

Suga, T., Takei, Y., & Hanawa, K. (1997). Thermostad Distribution in the North Pacific Subtropical Gyre: The Central Mode Water and the Subtropical Mode Water. Retrieved from https://journals.ametsoc.org/view/journals/phoc/27/1/1520-0485_1997_027_0140_tditnp_2.0.co_2.xml

Suga, T., Motoki, K., Aoki, Y., & Macdonald, A. M. (2004). The North Pacific Climatology of Winter Mixed Layer and Mode Waters. Retrieved from https://journals.ametsoc.org/view/journals/phoc/34/1/1520-0485_2004_034_0003_tnpcow_2.0.co_2.xml

Takatani, Y., Sasano, D., Nakano, T., Midorikawa, T., & Ishii, M. (2012). Decrease of dissolved oxygen after the mid-1980s in the western North Pacific subtropical gyre along the 137°E repeat section. *Global Biogeochemical Cycles*, *26*(2). https://doi.org/10.1029/2011GB004227

Takeshita, Y., Martz, T. R., Johnson, K. S., Plant, J. N., Gilbert, D., Riser, S. C., et al. (2013). A climatology-based quality control procedure for profiling float oxygen data. *Journal of Geophysical Research: Oceans*, *118*(10), 5640–5650. https://doi.org/10.1002/jgrc.20399

Udaya Bhaskar, T. V. S., Sarma, V. V. S. S., & Pavan Kumar, J. (2021). Potential Mechanisms Responsible for Spatial Variability in Intensity and Thickness of Oxygen Minimum Zone in the Bay of Bengal. *Journal of Geophysical Research: Biogeosciences*, *126*(6), e2021JG006341. https://doi.org/10.1029/2021JG006341

Winkler, L. W. (1888). Die Bestimmung des im Wasser gelösten Sauerstoffes. *Berichte Der Deutschen Chemischen Gesellschaft*, *21*(2), 2843–2854. https://doi.org/10.1002/cber.188802102122

Wolf, M. K., Hamme, R. C., Gilbert, D., Yashayaev, I., & Thierry, V. (2018). Oxygen Saturation Surrounding Deep Water Formation Events in the Labrador Sea From Argo-O_2 Data. *Global Biogeochemical Cycles*, *32*(4), 635–653. https://doi.org/10.1002/2017GB005829

Yasuda, I. (2004). North Pacific Intermediate Water: Progress in SAGE (SubArctic Gyre Experiment) and Related Projects. *Journal of Oceanography*, *60*(2), 385–395. https://doi.org/10.1023/B:JOCE.0000038344.25081.42

You, Y. (2003). The pathway and circulation of North Pacific Intermediate Water. *Geophysical Research Letters*, *30*(24). https://doi.org/10.1029/2003GL018561